

Facile Route for 3D Printing of Transparent PETg-Based Hybrid Biomicrofluidic Devices Promoting Cell Adhesion

Viraj Mehta, Sukanya Vilikkathala Sudhakaran, and Subha Narayan Rath*



Cite This: *ACS Biomater. Sci. Eng.* 2021, 7, 3947–3963



Read Online

ACCESS |

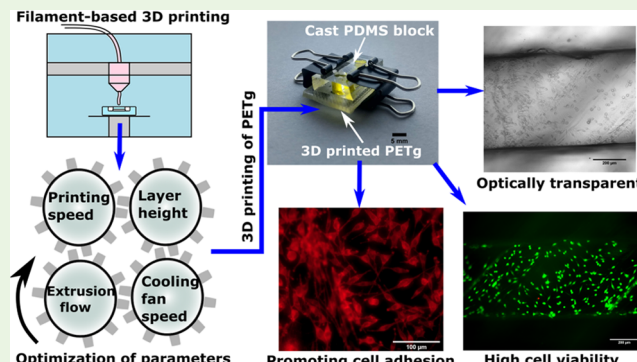
Metrics & More

Article Recommendations

Supporting Information

ABSTRACT: 3D printing has emerged as a promising fabrication technique for microfluidic devices, overcoming some of the challenges associated with conventional soft lithography. Filament-based polymer extrusion (popularly known as fused deposition modeling (FDM)) is one of the most accessible 3D printing techniques available, offering a wide range of low-cost thermoplastic polymer materials for microfluidic device fabrication. However, low optical transparency is one of the significant limitations of extrusion-based microfluidic devices, rendering them unsuitable for cell culture-related biological applications. Moreover, previously reported extrusion-based devices were largely dependent on fluorescent dyes for cell imaging because of their poor transparency. First, we aim to improve the optical transparency of FDM-based microfluidic devices to enable bright-field microscopy of cells. This is achieved using (1) transparent polymer filament materials such as poly(ethylene terephthalate) glycol (PETg), (2) optimized 3D printing process parameters, and (3) a hybrid approach by integrating 3D printed microfluidic devices with cast poly(dimethylsiloxane) (PDMS) blocks. We begin by optimizing four essential 3D printing process parameters (layer height, printing speed, cooling fan speed, and extrusion flow), affecting the overall transparency of 3D printed devices. Optimized parameters produce exceptional optical transparency close to 80% in 3D printed PETg devices. Next, we demonstrate the potential of FDM-based 3D printing to fabricate transparent micromixing devices with complex planar and nonplanar channel networks. Most importantly, cells cultured on native 3D printed PETg surfaces show excellent cell attachment, spreading, and proliferation during 3 days of culture without extracellular matrix coating or surface treatment. Next, we introduce L929 cells inside hybrid PETg-PDMS biomicrofluidic devices as a proof of concept. We demonstrate that 3D printed hybrid biomicrofluidic devices promote cell adhesion, allow bright-field microscopy, and maintain high cell viability for 3 days. Finally, we demonstrate the applicability of the proposed fabrication approach for developing 3D printed microfluidic devices from other FDM-compatible transparent polymers such as polylactic acid (PLA) and poly(methyl methacrylate) (PMMA).

KEYWORDS: 3D printing, transparency, microfluidic device, PETg, biocompatibility, cell adhesion



1. INTRODUCTION

Microfluidic devices enable the coculture of cells, dynamic exchange of nutrients, control over pressure and flow rate, and application of various mechanical forces, recapitulating some of the important aspects of organs. Hence, they have been used for organ and disease modeling *in vitro*.¹ Apart from organ modeling, microfluidic devices offer an affordable and reliable solution for anticancer drug testing and screening owing to the minimal utilization of cells and reagents.^{2,3} Soft lithography is considered the gold standard for fabricating such poly(dimethylsiloxane) (PDMS)-based microfluidic devices. Soft lithography uses photolithography for fabricating master molds. Photolithography can fabricate features less than 20 μm .^{4,5} However, it requires significant prior experience, time-consuming steps, and a cleanroom environment.

3D printing of microfluidic devices has been gaining popularity for the last 6 years due to its unprecedented rapid fabrication ability.⁶ 3D printers can fabricate monolithic microfluidic devices with nonplanar channel networks without multilayer bonding and alignment, previously unattainable with the soft lithography technique.^{7–9} One of the significant benefits of 3D printing over soft lithography is the rapid fabrication and testing of various design modifications in the initial prototyping phase of microfluidic devices. However, 3D printed devices

Received: May 11, 2021

Accepted: July 8, 2021

Published: July 20, 2021



generally suffer from lower optical transparency, lower gas permeability, higher cytotoxicity, and higher surface roughness than soft lithography-based PDMS microfluidic devices.⁶

Filament-based polymer extrusion (popularly known as fused deposition modeling (FDM)) is a low-cost and one of the most accessible 3D printing techniques, offering a wide range of thermoplastic polymer filament materials for microfluidic device fabrication. However, FDM-based microfluidic devices greatly suffer from low optical transparency. Therefore, previously reported polylactic acid (PLA) and acrylonitrile butadiene styrene (ABS)-based FDM microfluidic devices have been used for stem-cell encapsulation in alginate droplets,¹⁰ analytical applications,^{11,12} micromixing,¹³ droplet generation,¹⁴ and nano-particle synthesis¹⁵ but remain largely unexplored for cell culture-related biological applications. Few previous studies, which reported cell culture were mostly dependent on fluorescent dyes for cell imaging, mainly due to poor transparency of the devices.^{16,17} Dependency on fluorescent markers is often inconvenient for visualizing cells during the experiment in microfluidic devices because of photobleaching and image contrast errors. Hence, we first aim to improve the optical transparency of filament-based polymer extrusion microfluidic devices to enable bright-field microscopy of cells.

Poly(ethylene terephthalate) glycol (PETg) is one of the compatible polymers with FDM 3D printing. PETg is synthesized by replacing ethylene glycol groups of poly(ethylene terephthalate) (PET) with 1,4-cyclohexanedimethanol (CHDM) groups.¹⁸ Despite its excellent natural optical transparency and 3D printability, PETg has been used only in a few microfluidics-related applications such as fuel cell fabrication, micromixing, and droplet generation.^{19,20} Moreover, 3D printed PETg microfluidic devices are yet to be evaluated for cell culture-related biological applications. Therefore, we have selected PETg for fabricating microfluidic devices in the present study.

One of the reasons behind the low transparency of FDM-based devices is poor interlayer adhesion and air bubble entrapment.^{20,21} Previous studies indicated that optimization of the printing speed and layer height improved the optical transparency of 3D printed samples, thereby reducing the air bubble entrapment.^{10,22} However, the influence of other significant 3D printing parameters such as extrusion flow and cooling fan speed is yet to be explored. Apart from optimizing process parameters, previous reports implemented a hybrid approach by integrating 3D printed open microchannels (without roof layers) with optically transparent materials such as poly(methyl methacrylate) (PMMA) and glass coverslips.^{12,13,23} However, they did not demonstrate cell culture study or bright-field imaging inside 3D printed hybrid microfluidic devices. In the present study, we implement a hybrid approach by integrating cast PDMS blocks with 3D printed open channel PETg microfluidic devices using temporary (with binder clips) and permanent (with bis-amino silane) bonding protocols.

In the present study, we hypothesize that (1) optimization of 3D printing process parameters (layer height, printing speed, extrusion flow, and cooling fan speed) will improve the optical transparency of 3D printed PETg microfluidic devices by eliminating air voids, (2) 3D printed native surface will influence cell adhesion due to roughness, and (3) integrating gas-permeable PDMS blocks with gas-impermeable 3D printed microchannels will maintain higher cell viability inside hybrid devices than 3D printed monolithic thermoplastic devices

(channels printed inside polymer and sealed with roof layers). The gas permeability of various thermoplastic polymers is significantly lower than PDMS gas permeability.²⁴ Therefore, fixing PDMS blocks on the top of gas-impermeable polymer microchannels may support long-term cell culture, maintaining higher cell viability than 3D printed monolithic thermoplastic devices.

First, we optimize four essential 3D printing process parameters (layer height, printing speed, extrusion flow, and cooling fan speed) for improving the optical transparency of 3D printed devices. Dimensional accuracy of printed channels was also considered in the optimization process of extrusion flow and cooling fan speed as they may change the channel dimensions significantly. Using optimized parameters, we demonstrated the capability of FDM 3D printing to fabricate transparent micromixing devices with complex planar and nonplanar channel networks. The effect of UV/ozone surface activation on 3D printed PETg was also studied to control the wettability of microfluidic devices. Next, we evaluate the biocompatibility of 3D printed PETg with L929 mouse fibroblast cell line. The influence of surface roughness on cell adhesion was also studied. L929 cells were cultured for 3 days inside 3D printed PETg microfluidic devices to validate the proposed fabrication approach with optimized parameters and hybrid concept. Cell viability, cell adhesion, and cell visibility in bright-field microscopy were evaluated inside biomicrofluidic devices. We also introduced cells in 3D printed monolithic devices (channels printed inside PETg and sealed with roof layers) for comparison with hybrid biomicrofluidic devices. Finally, we demonstrated the applicability of the proposed fabrication approach for developing 3D printed microfluidic devices from other transparent FDM-compatible polymers such as PLA and PMMA.

2. MATERIALS AND METHODS

2.1. 3D Printing. 3D printing was carried out with a Hydra 200 pro system (ReddX Technologies Pvt. Ltd., Chennai, India). Hydra 200 has a positioning precision of 11 μm in XY and 2.5 μm in the Z-axis. Computer-aided design (CAD) modeling was carried out with Autodesk Inventor 2019 student edition (Autodesk Inc., California). Ultimaker Cura 4.0.0 (Ultimaker, Geldermalsen, Netherlands) was used for producing G-code out of STL files. 3D printing was carried out with 1.75 mm PETg (eSUN, Shenzhen, China), PLA (eSUN, Shenzhen, China), and PMMA (WOL3D, Mumbai, India) clear filaments with a 0.4 mm nozzle using an optimized set of parameters. Except four process parameters to be optimized in this study (layer height, printing speed, extrusion flow, and cooling fan speed), other 3D printing parameters were kept constant, as mentioned in Table 1.

2.2. Optimization Process of 3D Printing Parameters with PETg. We considered four 3D printing parameters (layer height, printing speed, extrusion flow, and cooling fan speed), affecting the

Table 1. Constant Parameters for 3D Printing

parameter	value
extruder temperature (as recommended by the manufacturer)	250 °C for PETg 250 °C for PMMA 220 °C for PLA
printing bed temperature (as recommended by the manufacturer)	80 °C for PETg 80 °C for PMMA 50 °C for PLA
infill density	100%
infill pattern (toolpath)	zigzag (45°)
nozzle diameter	0.4 mm

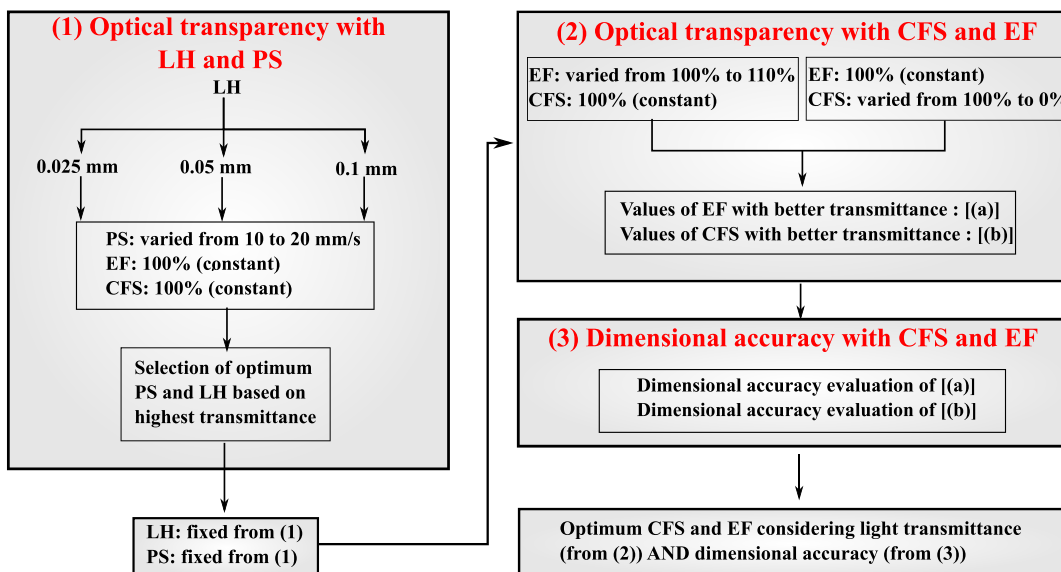


Figure 1. Optimization process of 3D printing parameters for improving transparency of microfluidic devices (LH = layer height, PS = printing speed, EF = extrusion flow, CFS = cooling fan speed).

optical transparency of 3D printed samples. The 3D printer builds components layer-by-layer. Each layer has a specific thickness indicated by layer height or layer thickness. The printing speed is the speed at which the printing head moves for material deposition. The extrusion flow is the amount of material extruded over a specific path in unit time (volume of material/time). For instance, assuming the cross-sectional shape of the deposited filament as rectangular, the volume of the material that needs to be extruded from the nozzle over a specific path length is given by the below-mentioned formula

$$\begin{aligned} \text{extrusion flow} &= \text{volume extruded in unit time} \\ &= \text{layer height} \times \text{extrusion width} \times \text{path length} \end{aligned}$$

By default, extrusion flow is considered as 100% in Cura (G-code producing software), suggesting the amount of material extruded over a specific path length will be the same as calculated by the software. The extrusion flow can be specified higher than 100% to extrude excess material from the calculated amount by the G-code producing software. Considering the layer height and path length as constant, changing extrusion flow will directly influence the extrusion width.

Two cooling fans are aimed at the build plate to solidify the extruded molten plastic material partially. By default, Cura sets the cooling fan speed at 100%, suggesting that the cooling fans will run at maximum speed during printing. The cooling fan speed can be specified below 100% to control the extruded molten plastic's cooling rate partially.

Figure 1 shows the optimization process for improving the optical transparency of 3D printed samples. We begin by evaluating the effect of layer height and printing speed, keeping extrusion flow and cooling fan speed at their default values. We chose three different layer heights for our experiments: 0.025, 0.05, and 0.1 mm. For each layer height, we varied the printing speed from 10 to 20 mm/s with a step size of 2 mm/s. The optimum values of the layer height and printing speed, providing the highest optical transparency, were used for the second experiment. In the second experiment, we evaluate the effect of extrusion flow and cooling fan speed on the transparency of 3D printed samples. First, extrusion flow was varied from default 100 to 110% (keeping the cooling fan speed at constant 100% and step size of 2%) and light transmittance from the sample was compared with control. Similarly, the cooling fan speed was varied from default 100 to 0% (keeping extrusion flow at constant 100% and step size of 20%) and light transmittance was compared with control. The control was printed with default values of extrusion flow (100%) and cooling fan speed (100%). At the end of the second experiment, we obtained the values of extrusion flow and cooling fan speed, providing better optical

transparency than control. Next, the settings for extrusion flow and cooling fan speed producing better optical transparency were further evaluated for their dimensional accuracy. The settings producing a nonsignificant variation in the channel width compared to control were finalized. The control was printed with default values of extrusion flow (100%) and cooling fan speed (100%). Thus, the settings for extrusion flow and cooling fan speed were decided based on optical transparency and dimensional accuracy for 3D printing of microfluidic devices.

2.3. Evaluation of Optical Transparency. Cylindrical devices with a diameter of 15 mm and a height of 1.5 mm were 3D printed from PETg, PMMA, and PLA by varying four main parameters, as mentioned before. The cylindrical devices were kept in 24-well plates, and absorbance values were recorded in a microplate reader (Enspire multimode plate reader, PerkinElmer, Massachusetts) between 350 and 750 nm. The absorbance values were converted to transmittance, according to eq 1.²⁵ The results were plotted at 550 nm, at which the human eyes are the most sensitive.¹⁰

$$T = \frac{I}{I_0} = 10^{-A} \quad (1)$$

where A = absorbance, I = intensity of light transmitted from the sample, I_0 = intensity of the original light, T = transmittance.

2.4. Evaluation of Dimensional Accuracy. Rectangular devices containing square channels of 0.5 mm were designed in Autodesk Inventor software. They were 3D printed from PETg by varying the extrusion flow from 100 to 110% (keeping the cooling fan speed constant at 100%) and cooling fan speed from 100 to 0% (keeping the extrusion flow constant at 100%). The layer height and printing speed were kept constant at the optimum values in both experiments. The square channels were made without roof layers on the top. Green food color dye was injected into the channels and imaged in an EVOS M7000 optical microscope (Thermo Fisher Scientific, Waltham, MA). The actual dimensions of printed channels were measured using ImageJ software and compared with the designed width of 500 μm .

2.5. Profilometry. Cylindrical devices with an overall diameter of 9.8 mm and height of 1.5 mm were 3D printed from PETg with three different layer heights: 0.025, 0.05, and 0.1 mm (keeping the other three parameters at optimum values). A 3D laser scanning microscope (LEXT OLS4000, Olympus Corporation, Japan) was used to obtain 3D surface topography and surface roughness parameters such as arithmetical mean height (S_a) and root-mean-square height (S_q) with a scanning area of $1287 \times 1291 \mu\text{m}^2$.

2.6. Characterization of Mixing Performance of 3D Printed Micromixers. Using an optimized set of process parameters, we 3D

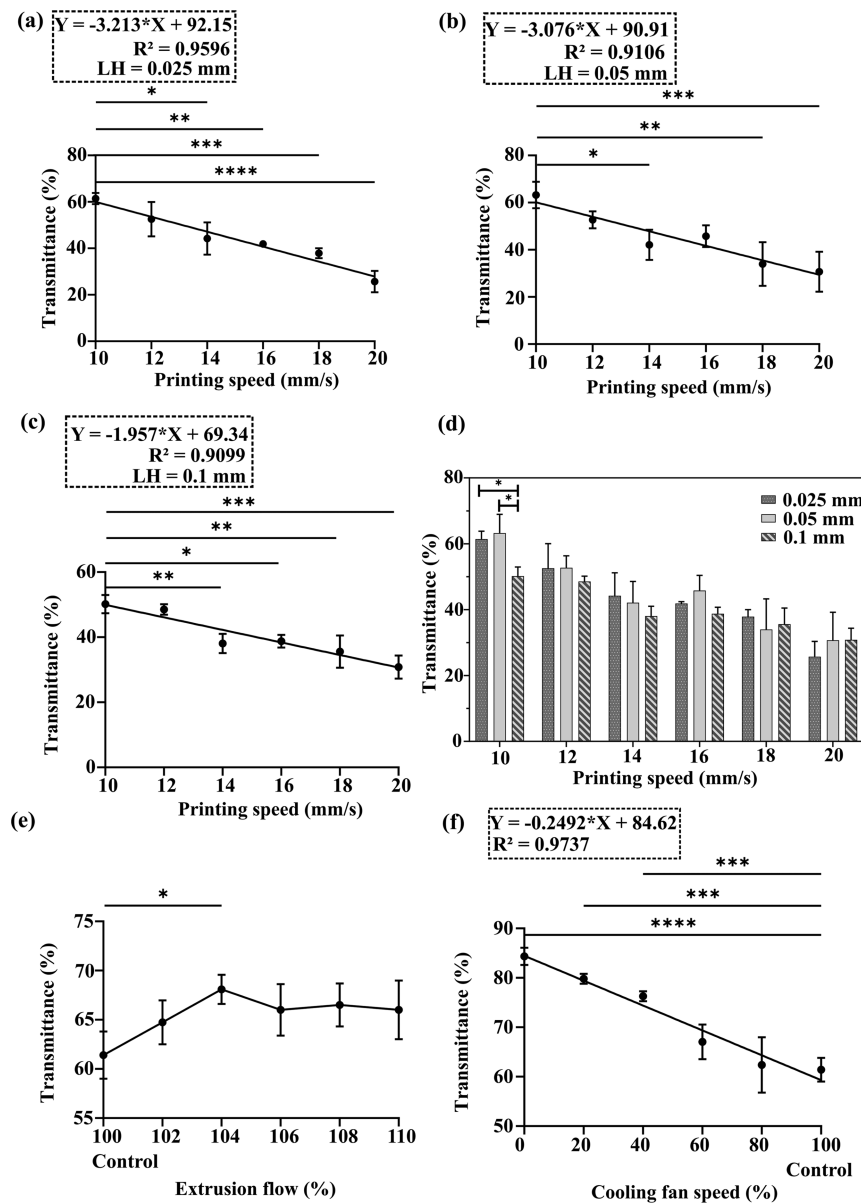


Figure 2. Influence of four process parameters on optical transparency of PETg samples at 550 nm: (a) influence of printing speed at 0.025 mm layer height, (b) influence of printing speed at 0.05 mm layer height, (c) influence of printing speed at 0.1 mm layer height, (d) influence of layer height at constant printing speed, (e) influence of extrusion flow, and (f) influence of cooling fan speed (LH = layer height).

printed various microfluidic mixers, including a T mixer, a serpentine mixer, and a 3D mixer from PETg. All mixers were designed with semielliptical microchannels with a major axis of 0.7 mm and a minor axis of 0.35 mm. We temporarily bonded cast PDMS blocks on top of 3D printed micromixers, as described in Section 2.13. The syringe pump (Chemex Inc., Stafford, TX) and Tygon silicon tubes (Achira Labs Pvt. Ltd., Bangalore, India) were used to perfuse water and 0.1% (v/v) blue food color dye solution (in water) from the two inlets at 10 $\mu\text{L}/\text{min}$. The absorbance values for blue dye at the inlet and diluted blue dye at the outlet of micromixers were measured using a microplate reader between 400 and 700 nm. Moreover, for visualizing the mixing process, the optical images of micromixers were taken in a microscope with two different color dyes (0.2% yellow and 0.1% blue) perfused at 10 $\mu\text{L}/\text{min}$.

2.7. Characterization of the Effect of UV/Ozone Treatment on PETg. PETg samples with length 30 mm, width 12.5 mm, and height 1.5 mm were printed with an optimized set of parameters. They were treated with UV/ozone (Novascan, Ames, IA) for 0, 15, and 30 min at room temperature at a distance of 2 cm from a UV lamp source. To characterize the effect of the same, contact angles of 10 μL of

deionized (DI) water droplets were measured with the help of a contact angle goniometer (Rame-Hart Instrument Company, Succasunna, NJ, Model 290-F4). Similarly, the contact angles were measured on the samples, soaked in DI water, 70% ethanol, and Dulbecco's modified Eagle's medium (DMEM, PAN Biotech, India) complete culture medium for 30 min immediately after UV/ozone treatment to check its surface stability.

2.8. Cell Culture. L929 mouse fibroblast cells (NCCS, Pune, India) were cultured in T75 tissue culture flasks using high-glucose Dulbecco's modified Eagle's medium (DMEM, PAN Biotech, India) supplemented with 10% fetal bovine serum (FBS, Sigma-Aldrich, India) and 1% antibiotic-antimycotic solution (penicillin-streptomycin, Invitrogen, Thermo Fisher Scientific, India) and maintained in an incubator (Thermo Scientific Forma Series-3131, India) at standard conditions (37 °C, 5% CO₂, and 95% humidity). The culture medium was changed every 48 h. The cells were trypsinized (0.25% Trypsin-EDTA, Sigma-Aldrich, India) at 80% confluence and used for the experiments.

2.9. Cell Seeding on Cylindrical Devices for Biocompatibility Evaluation. Cylindrical devices with an overall diameter of 9.8 mm and a height of 1.7 mm were 3D printed from PMMA, PETg, and PLA

with optimized parameters. Subsequently, the devices were sterilized with 70% ethanol, rinsed with 1× phosphate-buffered saline (PBS), placed in 48-well plates, and air-dried for 2 h in an incubator at 37 °C. Fifteen thousand cells were seeded on the cylindrical devices (30 μL of cell suspension). The cell-seeded devices were incubated at standard conditions for 90 min to allow cell attachment before adding 500 μL of complete culture medium. Next, the devices were cultured at standard conditions for 72 h. The optical images of the cells were taken in the EVOS M7000 optical microscope.

2.10. Live/Dead Assay. The live/dead assay was performed with fluorescein diacetate (FDA)/propidium iodide (PI) fluorescent staining to evaluate cell viability on cylindrical devices and 3D printed biomicrofluidic devices. First, 2 μg/mL FDA (Molecular Probes Inc., Eugene) and 20 μg/mL PI (Invitrogen, India) 20 μg/mL were prepared in 1× PBS. Next, the devices were rinsed with PBS and incubated with FDA solution for 15 min. After rinsing with PBS, they were stained with PI at room temperature for 2 min. After a gentle wash with PBS, the devices were viewed under the EVOS M7000 fluorescent microscope. Quantification of the live/dead assay was carried out with ImageJ software by calculating the percentage area fraction of live cells (green) and dead cells (red).²

2.11. Cytoskeleton and Cell Nuclei Staining. Actin was stained with Alexa Fluor-647 phalloidin (A22287, Life Technologies), and cell nuclei were stained with SYTOX Green (S33025, Life Technologies). The cells were first fixed using 4% paraformaldehyde in 1× PBS for 30 min. This was followed by permeabilization of cell membrane using 0.1% (w/v) Triton X-100 in 1× PBS for 5 min and blocking in 1% (w/v) bovine serum albumin (BSA) for 10 min. Next, the 3D printed samples were incubated with Alexa Fluor-647 phalloidin in 0.1% BSA (1:20) for 45 min at room temperature to stain the actin cytoskeleton. Subsequently, they were incubated with SYTOX Green in phosphate-free buffer (1:300) for 10 min. Finally, the cells were viewed under a fluorescent microscope (Carl Zeiss Apotome.2, Germany).

2.12. Fabrication of Microfluidic Devices from PETg. Two types of microfluidic devices were fabricated using optimized parameters: (1) monolithic (with channel embedded inside) and (2) open channel devices (hybrid devices). The overall dimensions of the monolithic microfluidic devices were 26.5 mm (length) × 16 mm (width) × 2 mm (height). A semielliptical microchannel with a major axis of 0.7 mm and a minor axis of 0.35 mm was printed within PETg monolithic device using optimized parameters. Roof layers were printed on top of the semielliptical channel to seal it.

In hybrid devices, except for height (1.8 mm), the length and width were kept the same as monolithic devices. An open microchannel with a square cross section of 0.7 mm was printed and sealed with the PDMS block from the top containing inlets and outlets, as described in Section 2.13.

2.13. Temporary and Permanent Bonding of PETg with PDMS. A solution of PDMS base and curing agent (Sylgard 184, Dow Chemical International Pvt. Ltd., India) was prepared with 10:1 (w/w) ratio. Subsequently, it was degassed and poured over the Petri dish. The Petri dish was heated at 60 °C overnight to cure the PDMS. The PDMS blocks were cut according to the dimensions of 3D printed PETg microfluidic devices, and holes were punched in them using a 4 mm biopsy punch (Well Tech, Taiwan). Binder clips (15 mm) were used to attach PDMS on the top of 3D printed PETg devices for temporary bonding.

The PETg devices were permanently bonded to PDMS using bis-amino silane treatment, similarly to the previously reported protocol with a few changes.²⁶ First, 3D printed PETg devices were treated with a UV/ozone cleaner (Novascan, Ames, IA) for 30 min. At the same time, previously prepared PDMS blocks were treated with a 30 W plasma cleaner (Harrick Plasma, Ithaca, NY) for 2 min. Next, PETg devices were treated with a solution of 2% bis[3-(trimethoxysilyl)propyl]amine (bis-amino silane) (TCI Chemicals, Tokyo, Japan), 97% isopropyl alcohol, and 1% deionized water at 70 °C for 20 min on a hot plate. Subsequently, they were immersed in isopropyl alcohol for 10 min and heated at 70 °C in a hot air oven for 30 min. Next, the devices were treated with 70% ethanol for 30 min. Finally, the plasma-treated PDMS

blocks were brought into contact with the PETg surfaces and kept at 60 °C in a hot air oven overnight for bonding.

2.14. Cell Seeding Inside Hybrid and Monolithic Biomicrofluidic Devices. Firstly, 3D printed PETg microfluidic devices were sterilized with 70% ethanol, rinsed with 1× PBS, placed in a 100 mm Petri dish, and air-dried for 2 h in an incubator at 37 °C. In hybrid devices, PDMS blocks were placed on the top of 3D printed PETg microfluidic devices and temporarily bonded using binder clips. Next, monolithic and hybrid devices were filled with 90 μL of complete culture medium. Ten thousand cells (20 μL cell suspension) were seeded inside each microfluidic device. The devices were cultured at standard conditions for 3 days. On day 3, the cells were stained with FDA/PI as described in Section 2.10 and imaged under EVOS M7000 fluorescent microscope. Mean cell circularity was measured from FDA/PI images to confirm the cell morphology using ImageJ.²⁷ A circularity of 1.0 indicates a perfect circle.

2.15. Statistical Analysis. All data are expressed as mean ± SD (standard deviation) of three or five independent experiments (except profilometry). GraphPad Prism (GraphPad Software Inc., San Diego, CA) software was used to perform a one-way analysis of variance (ANOVA) followed by Bonferroni's posthoc to check the significance level. Significance was determined by $p < 0.05$ (*), $p < 0.01$ (**), $p < 0.001$ (***) $, and $p < 0.0001$ (****).$

3. RESULTS

3.1. Influence of Layer Height and Printing Speed on Optical Transparency. Figure 2a–c shows the influence of printing speed on the optical transparency of 3D printed PETg samples. The samples were printed with 0.025, 0.05, and 0.1 mm layer heights keeping cooling fan speed and extrusion flow constant at their default values (100%). First, visible light transmittance followed a linear trend with printing speed for each layer height. In general, 10 mm/s printing speed produced better optical transparency than printing speeds higher than 12 mm/s in all considered layer heights. Therefore, 10 mm/s printing speed was selected for subsequent experiments. Figure S1 shows a dramatic influence of printing speed on the transmittance of 3D printed samples in the visible light spectrum. Figure S2a also shows the notable variation in optical transparency with the printing speed in PETg samples.

Figure 2d shows the influence of layer height on optical transparency of 3D printed samples. The layer heights of 0.025 and 0.05 mm produced higher transparency than the 0.1 mm layer height at 10 mm/s printing speed. However, we did not find a notable influence of layer height on light transmittance for printing speeds higher than 10 mm/s. Moreover, layer heights of 0.025 and 0.05 mm did not produce a significant difference in light transmittance at 10 mm/s printing speed, suggesting either of the two layer heights can be used for microfluidic device fabrication. However, a reduction in layer height produces a lower staircase effect in printing inclined and curved surfaces.²⁸ Such a stair-stepping effect is believed to be present in micromixing devices (Section 2.6) and monolithic cell culture devices (Section 2.12) having semielliptical channels. Therefore, we selected the 0.025 mm layer height for the next set of experiments, reducing the overall staircase effect.

3.2. Influence of Extrusion Flow and Cooling Fan Speed on Optical Transparency. From Section 3.1, we obtained optimum values of layer height (0.025 mm) and printing speed (10 mm/s) based on light transmittance. In this section, we first begin with the optimization of extrusion flow, keeping the printing speed (10 mm/s), layer height (25 μm), and cooling fan speed (100%) constant. From Figure 2e, we found transmittance at 104% extrusion flow was significantly higher than control. However, extrusion flow higher than 104%

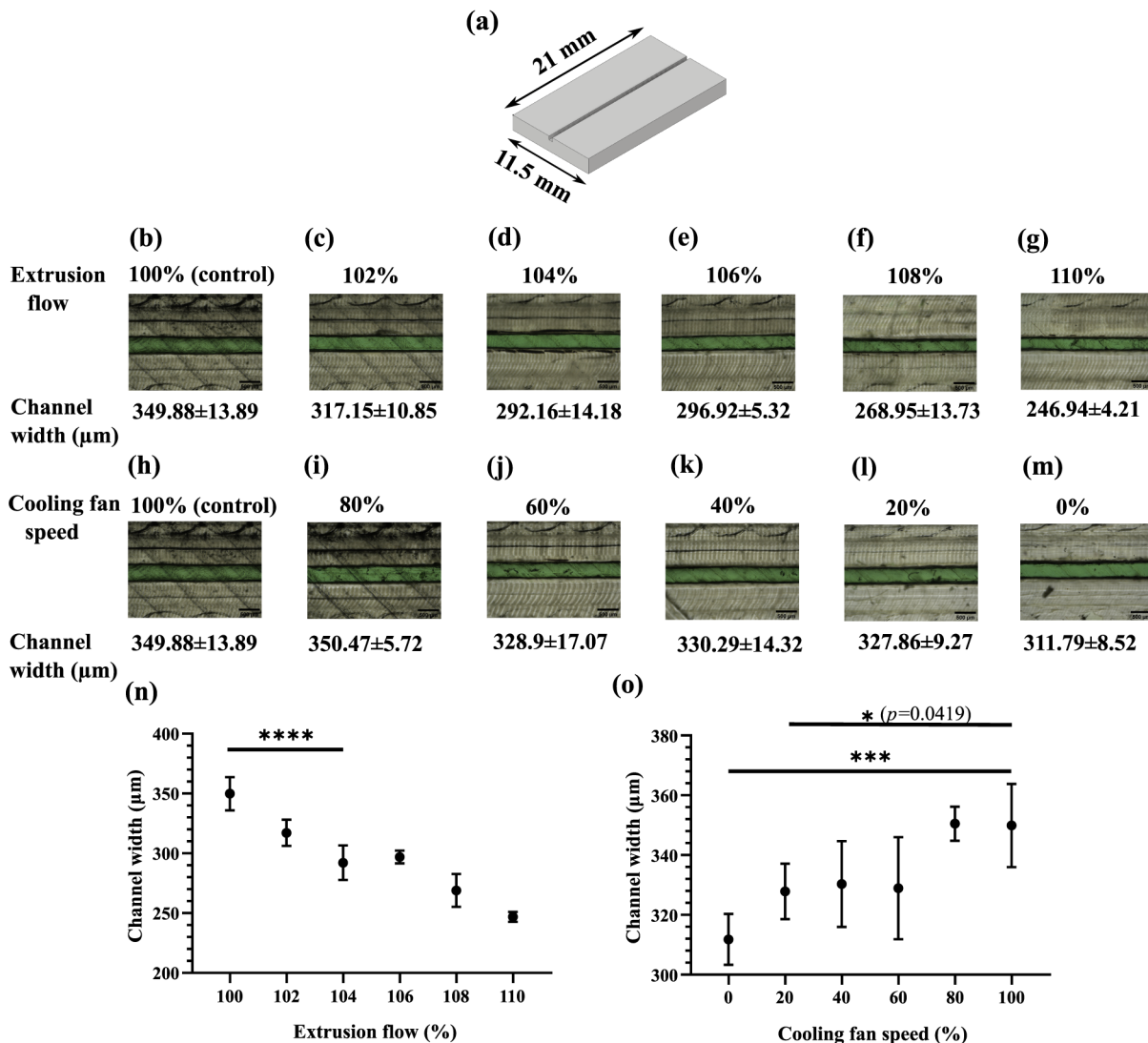


Figure 3. Measured width of 3D printed microchannels with a designed width of $500 \mu\text{m}$. (a) CAD model of the sample used for measurement, (b–g) measured width by varying extrusion flow, (h–m) measured width by varying the cooling fan speed, (n) plot of measured width by varying extrusion flow, and (o) plot of measured width by varying cooling fan speed.

did not produce better optical transparency than control. Therefore, it was concluded that the extrusion flow can be increased to 104% to improve optical transparency compared to control.

As shown in Figure 2f, transmittance follows a linear trend with a cooling fan speed. PETg samples printed with cooling fan speeds of 0, 20, and 40% were more transparent than the control, indicating that the cooling fan speed can be kept in the range of 0–40%. Moreover, optical transparency close to 80% was easily achievable with cooling fan speed $\leq 40\%$, which was previously unattainable.^{10,29} Eighty percent optical transparency of PETg is closer to optical transparency of conventional microfluidics materials such as PDMS and PMMA ($\sim 90\%$).^{29,30} Figure S2b,c shows the optical transparency of 3D printed PETg samples by varying the extrusion flow and cooling fan speed, respectively.

We suspected significant variation in channel width because of reduced cooling fan speed and increased extrusion flow from their default values. Therefore, in addition to light transmittance, dimensional variation in 3D printed microchannels was also measured before finalizing extrusion flow and cooling fan speed in Section 3.3.

3.3. Dimensional Accuracy of 3D Printed Microfluidic Channels.

The dimensions of the 3D printed microchannels often deviate from the designed dimensions in the material extrusion process.³¹ We suspected higher variations in channel dimensions with an increase in extrusion flow and a decrease in cooling fan speed. In this section, we have measured the width of 3D printed channels by varying the cooling fan speed and the extrusion flow keeping the layer height at $25 \mu\text{m}$ and printing speed at 10 mm/s .

Figure 3a shows the CAD model of the device with a microchannel used for this study. Figure 3b–g shows the width of 3D printed microchannels deviated from the designed channel width of $500 \mu\text{m}$ when extrusion flow was increased from 100 to 110%. The control shows $\sim 150 \mu\text{m}$ average reduction in channel width from the designed channel width. Similarly, from Figure 3h–m, we observed a reduction in channel width from the designed channel width when the cooling fan speed was varied from 100 to 0%.

From the results of Section 3.2, it was decided to increase extrusion flow to 104% for better optical transparency. However, the channel width at 104% extrusion flow was significantly

different from the control ($p < 0.0001$) (Figure 3n). Therefore, we decided to keep extrusion flow at 100%, considering the high dimensional inaccuracy in the 3D printed microchannel at 104% extrusion flow from the control. Similarly, we decided to keep the cooling fan speed in the range of 0–40% from Section 3.2. We found that the channel dimensions with 0% ($p < 0.001$) and 20% ($p = 0.0419$) cooling fan speeds were significantly different from the control (Figure 3o). Therefore, we decided to keep the cooling fan speed at 40% for 3D printing of microfluidic devices.

Thus, by considering light transmittance (Section 3.2) and dimensional accuracy (Section 3.3), the extrusion flow and cooling fan speed were finalized. Optimized process parameters for 3D printing of microfluidic devices are mentioned in Table 2.

Table 2. Optimized Parameters for 3D Printing of Microfluidic Devices

parameter	value
layer height	0.025 mm
printing speed	10 mm/s
extrusion flow	100%
cooling fan speed	40%

Traditional zigzag infill patterns with angles of 0, 90, and 45° have been used widely in previous reports related to 3D printed microfluidic devices.^{10,20,29} Infill angles of 0, 90, and 45° produced similar optical transparency in the 3D printed samples with optimized parameters (Figure S3). However, alternate infill angles of (45, 135°) (odd layers with 45° and even layers with 135°) produced significantly lower optical transparency in 3D printed samples. Therefore, we selected an infill angle of 45° in all of the devices printed in this study. Figure S4 shows the schematic of the zigzag nozzle movement path (45°) for various 3D printed devices with 100% infill.

3.4. Profilometry. 3D printed components are inherently rough because of the extrusion process and layer-by-layer fabrication approach.^{32,33} Therefore, we first measured surface roughness parameters of printed samples by varying the layer height, which is one of the most influential parameters affecting the surface roughness of 3D printed samples.³³ We have kept other parameters constant at optimized values (cooling fan speed = 40%, extrusion flow = 100%, printing speed = 10 mm/s). Figure 4 shows the uneven surface topography for 0.025, 0.05, and 0.1 mm layer heights in 2D and 3D views. We found that 3D printing with 0.025 mm layer height produced lower average surface roughness ($S_a = 24.827 \mu\text{m}$) compared to the other two layer heights. Moreover, the root-mean-square height ($S_q = 35.058 \mu\text{m}$) was also found comparatively lower in the case of 0.025 mm layer height.

As the surface roughness also significantly impact the optical transparency of 3D printed samples, we observed the topography of 3D printed surfaces in bright-field microscopy (Figure S5). The observed sharkskinlike pattern on the 3D printed surface was significantly reduced with optimized parameters, thereby improving the optical transparency of the topmost 3D printed surface.

3.5. 3D Printed Micromixers. Using optimized parameters, we have demonstrated the capability of FDM 3D printing to fabricate transparent micromixing devices with complex planar and nonplanar channel networks in this section. The T mixer and serpentine mixer contain a planar channel network, and the 3D mixer was designed with a nonplanar channel network.

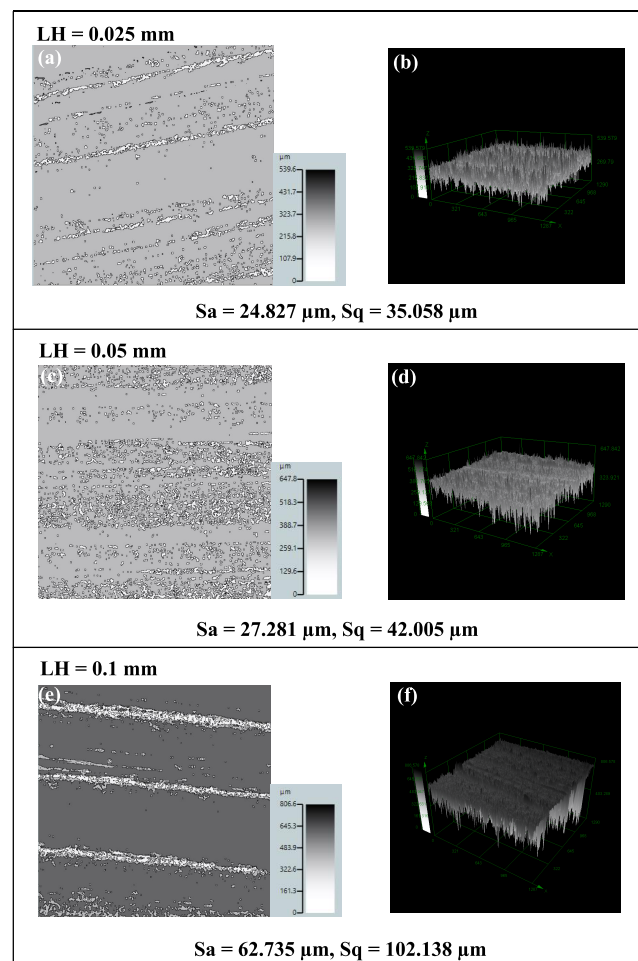


Figure 4. Surface topography and surface roughness parameters of 3D printed samples. (a, b) 2D and 3D views showing the height of features on the PETg sample printed with a layer height of 0.025 mm, (c, d) 2D and 3D views showing the height of features on the PETg sample printed with a layer height of 0.05 mm, and (e, f) 2D and 3D views showing the height of features on the PETg sample printed with a layer height of 0.1 mm (LH = layer height, S_a = arithmetical mean height, S_q = root-mean-square height).

The average printing time for each microfluidic device is 2 h 32 min (152 min) (Table S1), which is significantly lower than the average time required for fabricating a microfluidic device with soft lithography (~24 h) and close to the average time required with 3D printing (~2 h).³⁴ The same device can be printed within 2 h using a layer height of 50 μm with similar optical transparency (Figure 2d) but higher surface roughness (Figure 4) than devices printed with 25 μm layer height (keeping printing speed = 10 mm/s, extrusion flow = 100%, cooling fan speed = 40%).

Usually, channels with square cross sections contain a high bridging gap, leading to sagging of polymers. Therefore, we have used semielliptical channels to minimize the bridging gap and sagging of the roof.³¹ Figure S6 shows channels with elliptical and square cross sections with sagging of the roof in a square microchannel. Figure S7 shows the CAD models of the mixing devices with semielliptical microchannels. The distance between inlets and an outlet has been kept equal in all the mixers. However, each mixing device has an unequal mixing unit length, with the 3D mixer having the longest mixing unit length for diffusion.

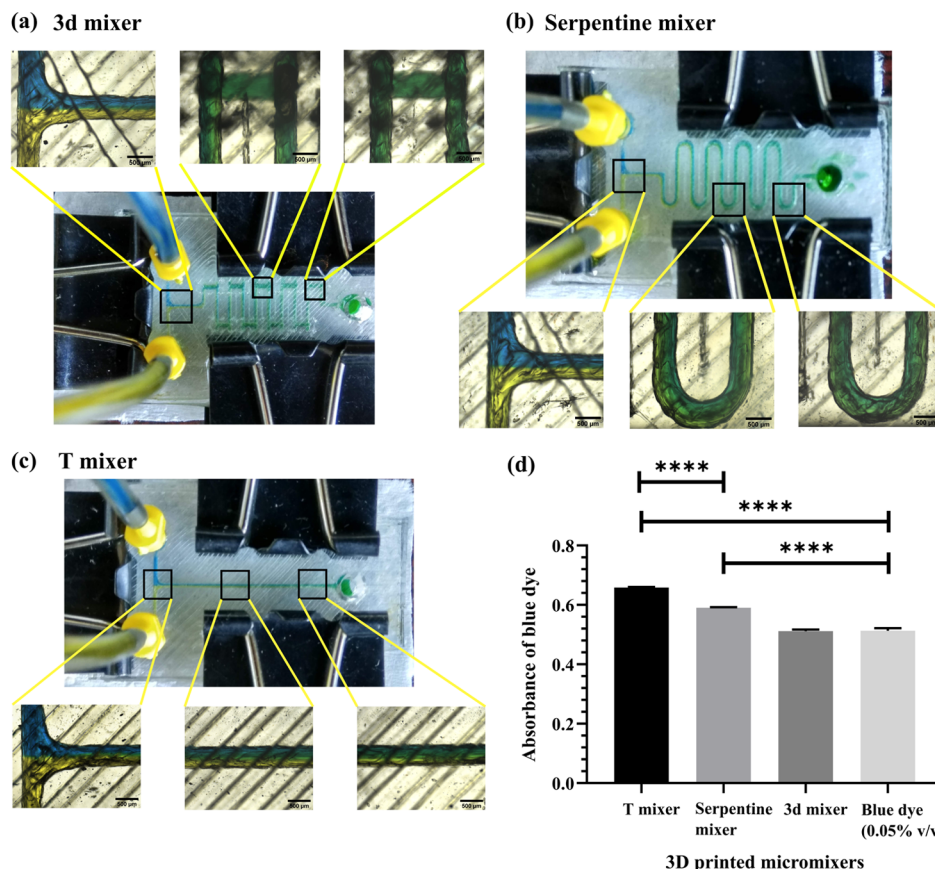


Figure 5. 3D printed micromixers: (a) 3D mixer, (b) serpentine mixer, (c) T mixer, and (d) quantification of mixing using a microplate reader.

Filament extrusion-based microfluidic devices are prone to fluid leakage due to poor interlayer fusion. However, 100% infill density and optimized parameters produced leak-free micromixers when perfused with blue dye (Figure S8). Moreover, elastomeric PDMS blocks fixed on top of 3D printed PETg devices ensured a leak-free connection of Tygon tube luer with the inlet and outlet of micromixers. Optical microscopy images taken at three locations of micromixers have been shown in Figure 5a–c. It was observed that the T mixer (Figure 5c) had the least mixing of blue and yellow dyes at the end.

For quantification of mixing, we perfused 0.1% (v/v) blue dye solution and water from the two inlets at a 10 $\mu\text{L}/\text{min}$ flow rate. According to the Beer–Lambert law (considering molar absorption coefficient and optical path length as constants)

$$A \propto c \quad (2)$$

where A = absorbance and c = concentration of blue dye.

$$\frac{A_i}{A_o} = \frac{c_i}{c_o} \quad (3)$$

where A_i = absorbance of blue dye at the inlet, A_o = absorbance of blue dye at the mixer outlet, c_i = concentration of blue dye at the inlet, and c_o = concentration of blue dye at the mixer outlet.

If the blue dye solution is completely diluted at the outlet, its concentration will be 0.05% (v/v), meaning $c_o = c_i/2$. If we substitute the same in eq 3

$$\frac{A_i}{2} = A_o \quad (4)$$

According to eq 4, we have compared the absorbance of the blue dye solution from the mixers' outlet with half of the absorbance

value of 0.1% (v/v) inlet blue dye (or 0.05% v/v blue dye) in Figure 5d. We considered maximum absorbance found at 630 nm for comparing the performances. We found that the 3D mixer produced a completely diluted blue dye solution, suggesting the highest mixing efficiency compared to the other two micromixers. The serpentine mixer and T mixer produced poor mixing of the blue dye solution at the outlet. However, the absorbance value of the serpentine mixer (0.5906 ± 0.001) was nearer to 0.05% blue dye (0.5129 ± 0.009) than that of the T mixer (0.6583 ± 0.0017). Therefore, the serpentine mixer was relatively better compared to the T mixer.

3.6. Characterization of the Effect of UV/Ozone Treatment.

It is important to have a hydrophilic polymer surface for rapid filling of fluids in 3D printed microchannels during biological experiments.³⁴ To decide UV/ozone treatment time for permanent bonding of PETg with PDMS, we have characterized the effect of the same on PETg.

Figure 6a shows the CAD model of a 3D printed PETg device used for contact angle measurements. The native 3D printed PETg surface has an apparent contact angle of $85 \pm 0.38^\circ$, close to the hydrophilic to hydrophobic transition region (Figure 6b). The surface becomes more hydrophilic, with an increase in time of UV/ozone treatment (Figure 6c,d). Moreover, 30 min of UV/ozone treatment produced a completely wet surface.

Microfluidic channels are often washed with three common fluids in biological experiments: (1) DI water, (2) ethanol, and (3) cell culture medium. Therefore, it is necessary to check the surface stability of UV/ozone treatment after washing with the mentioned fluids. Fifteen minutes of UV/ozone treatment keeps the contact angle stable at around $51.77 \pm 2.91^\circ$ for DI water, $52.43 \pm 1.88^\circ$ for ethanol, and $48.17 \pm 4.05^\circ$ for cell culture

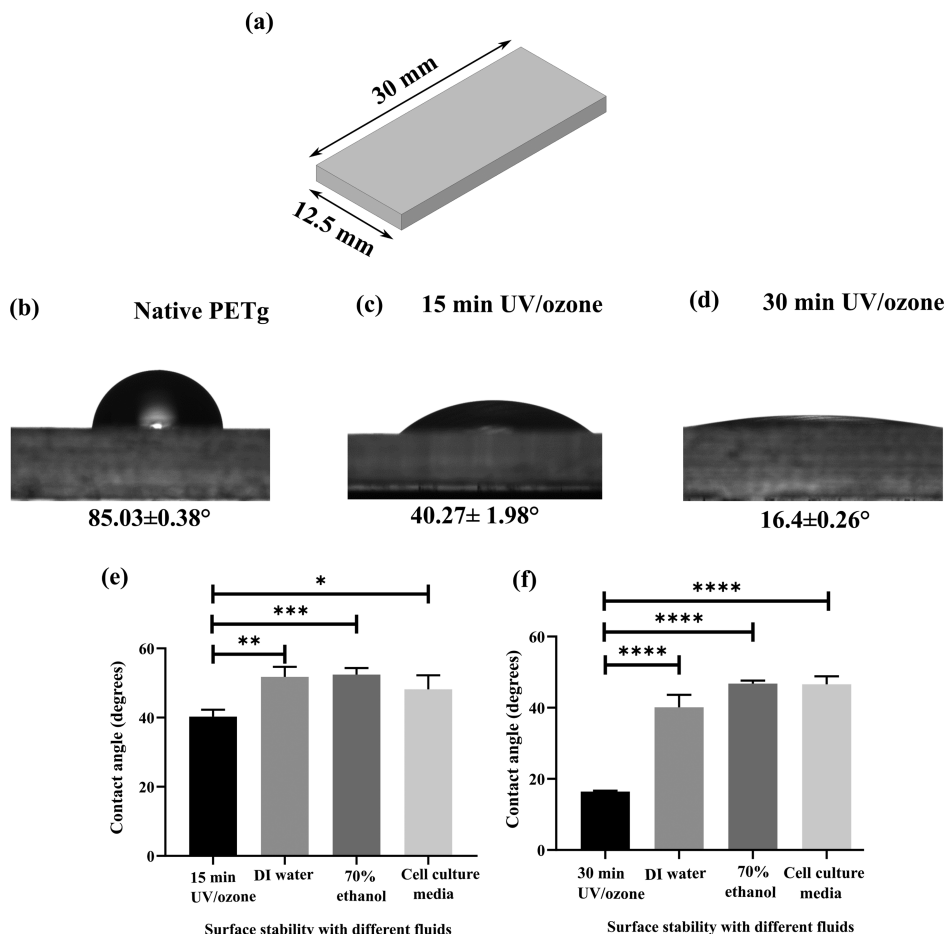


Figure 6. Characterization of the effect of UV/ozone treatment. (a) CAD model of the PETg device used for contact angle measurements, (b) contact angle on the native 3D printed PETg surface, (c) contact angle after 15 min of UV/ozone treatment, (d) contact angle after 30 min of UV/ozone treatment, (e) surface stability of 15 min UV/ozone treatment on PETg, and (f) surface stability of 30 min UV/ozone treatment on PETg.

medium (Figure 6e). Moreover, after 30 min of UV/ozone treatment, the contact angle remains stable at $40.1 \pm 3.53^\circ$ for DI water, $46.77 \pm 0.85^\circ$ for ethanol, and $46.57 \pm 2.26^\circ$ for cell culture medium (Figure 6f). We found that 30 min of UV/ozone treatment had higher stability than 15 min after washing with DI water ($p = 0.001$). However, cell culture medium and ethanol treatments did not show any significant difference between the two groups. Based on the results, we utilized 30 min of UV/ozone treatment time for activating the PETg surface for permanent bonding with PDMS.

3.7. Biocompatibility Evaluation and Effect of Roughness on Cell Adhesion. Previous reports suggest that the roughness of 3D printed samples has a pronounced effect on cell adhesion and spreading.^{35,36} Therefore, we evaluated the effect of surface roughness with the cylindrical devices printed with optimized parameters (Figure 7a). The topmost part of the device was designed with 0.8 mm thick walls with 0.7 mm height to prevent the cell suspension from leaking out of the PETg surface. We found L929 cells had mostly rounded morphology at the end of day 1 (Figure 7b). However, within 48 h, most of the cells appeared attached with spindle morphology distinctly visible (Figure 7c). The morphology of L929 cells cultured on PETg was found similar to the cells cultured on a standard tissue culture plate after 2 days (Figure 7d). We used actin staining for cytoskeleton assessment of cells cultured on 3D printed PETg devices. Figure 7e–g confirms the presence of intact actin filaments, indicating the structural integrity of cells on the

devices. Moreover, the cells were visible in bright-field imaging, demonstrating excellent optical transparency of 3D printed PETg with optimized parameters. We found that the optimization of parameters allowed better optical microscopy imaging of cells than the previously reported study.³¹ Live/dead staining on the PETg surface on day 3 shows a significant number of live cells and a few dead cells (Figure 7h,i), proving that the 3D printed PETg surface is biocompatible. In summary, despite the low wettability of PETg (Figure 6b), the 3D printed PETg surface allows cell attachment, spreading, and proliferation without extracellular matrix (ECM) coating or surface treatment.

3.8. Hybrid PETg-PDMS Biomicrofluidic Devices. After biocompatibility evaluation on the 3D printed PETg surface, we introduced the cells in 3D printed PETg-PDMS microfluidic devices as a proof of concept. We have also fabricated monolithic (with channel embedded inside) devices (Figure 8a) for comparison with hybrid devices (Figure 8b). The hybrid devices were fabricated with a channel having a square cross section of 0.7 mm instead of 0.5 mm. This is because of the average channel reduction of 170 μm with optimized parameters (Figure 3k). To compensate for 3D printing dimensional inaccuracy, we decided to increase the designed channel width by 200 μm , making it 700 μm for 3D printing biomicrofluidic devices. After increasing the channel width by 200 μm , we found the measured width of the 3D printed channel was $532.51 \pm$

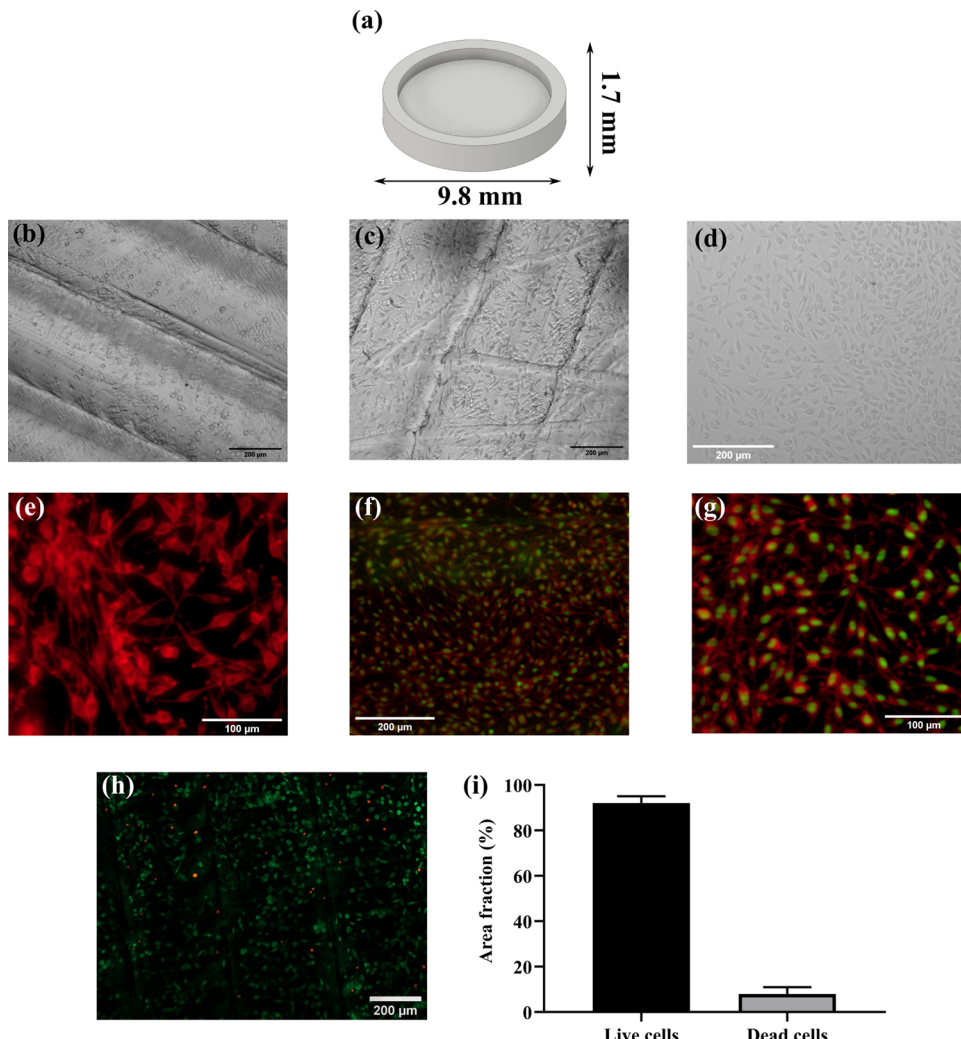


Figure 7. Biocompatibility evaluation and effect of surface roughness. (a) CAD model of the 3D printed device used for cell culture, (b) optical microscopy image of L929 cells on the PETg device on day 1, (c) optical microscopy image of L929 cells on PETg device on day 2, (d) optical microscopy image of L929 cells on tissue culture plate (control) on day 2, (e) actin staining of L929 cells on the 3D printed PETg device on day 2, (f) actin (red) and nuclei (green) staining of L929 cells on the 3D printed PETg device on day 2, (g) actin (red) and nuclei (green) staining of L929 cells on the 3D printed PETg device on day 2 at a higher magnification, (h) live/dead (green/red) staining (FDA/PI) on the 3D printed PETg device on day 3, and (i) quantification of live/dead staining on the 3D printed PETg device on day 3.

6.49 μm (Figure S9), close to the desired channel width of 500 μm .

The monolithic devices were fabricated with semielliptical microchannels with a major axis of 0.7 mm and a minor axis of 0.35 mm. A square cross section was not selected as it involves a larger bridging gap leading to sagging of the roof (as discussed in Section 3.5). Moreover, the roof layers printed on top of rectangular or square channels severely compromised the optical transparency of the microchannels (Figure S9). On the contrary, a channel printed with a semielliptical cross section with roof layers enhanced the channels' visibility compared to a square cross section (Figure S9). Therefore, we used semielliptical channels in monolithic devices.

UV/ozone treatment used in permanent bonding can affect cell adhesion due to low wettability.³⁷ Although a significant portion of generated oxidized material gets washed away, the wettability still remains between 40 and 46° for various fluids tested after 30 min of UV/ozone treatment (Figure 6f). Therefore, to check the cells' response on the native PETg surface, we decided to use a temporary bonding for hybrid

devices in the present study. Temporary bonding was leak-proof during 3 days of static cell culture. However, for long-term dynamic perfusion cell culture, PETg should be permanently bonded with PDMS to prevent potential fluidic leakage. Video S1 shows the blue dye perfusion inside a leak-proof permanently bonded hybrid microfluidic device at a 100 $\mu\text{L}/\text{min}$ flow rate.

A permanent bonding protocol using bis-amino silane was demonstrated previously for bonding PET membrane to PDMS for long-term cell culture.²⁶ We have demonstrated that the bis-amino silane chemical bonding protocol can also be applicable for bonding 3D printed PETg with PDMS. We have modified the previously reported protocol according to the properties of PETg: (1) instead of plasma treatment in PET, we have utilized 30 min of UV/ozone treatment in PETg for surface activation, (2) considering the low glass transition temperature of PETg, treatment with silane was carried out at 70 °C instead of previously reported 80 °C, and (3) assembled PETg-PDMS devices were kept overnight at 60 °C for bonding instead of keeping for 1 h at 70 °C.

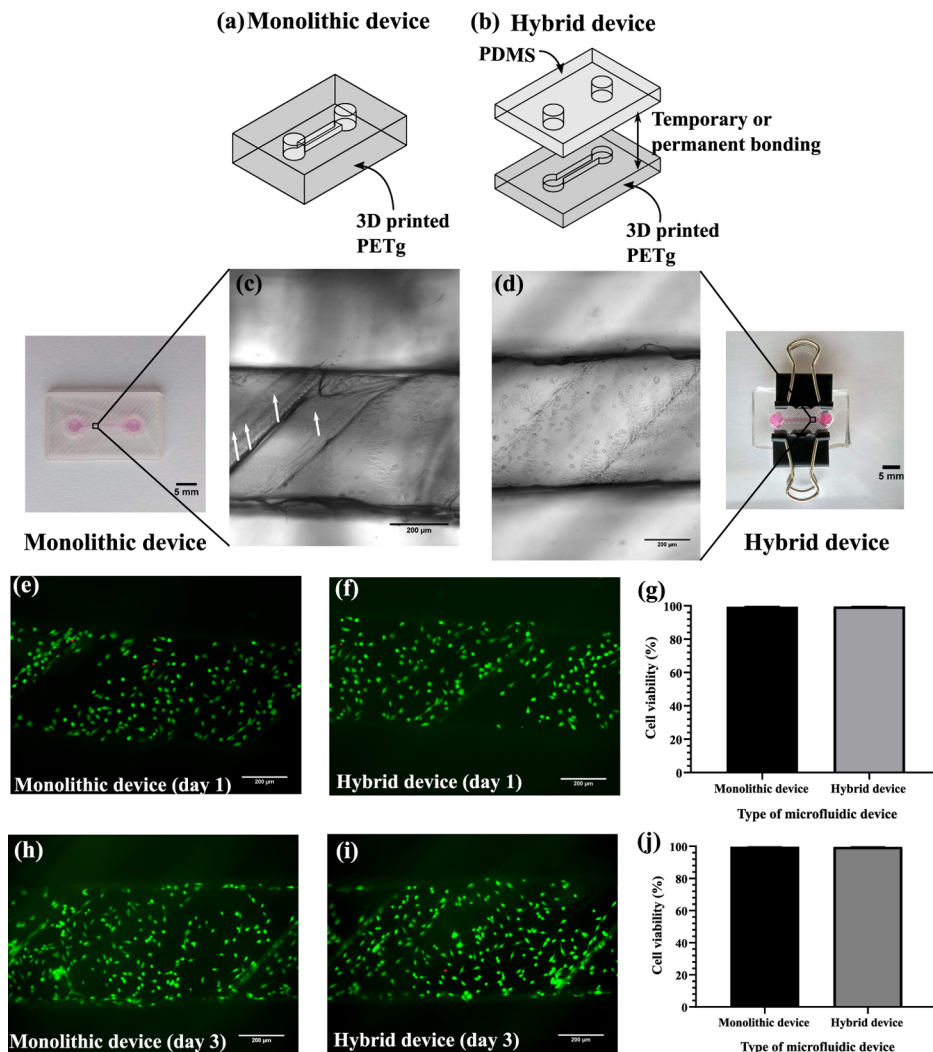


Figure 8. L929 fibroblasts cultured in monolithic (PETg) and hybrid (PETg-PDMS) microfluidic devices. (a, b) schematic of monolithic and hybrid devices, (c) optical microscopy image of L929 cells cultured in a monolithic device (white arrows show the barely visible cells in bright-field microscopy), (d) optical microscopy image of L929 cells cultured in the hybrid device, (e, f) live/dead staining (FDA/PI) of L929 cells cultured in a monolithic and hybrid microchannel on day 1, (g) quantification of cell viability on day 1, (h, i) live/dead staining (FDA/PI) of L929 cells cultured in a monolithic and hybrid microchannel on day 3, and (j) quantification of cell viability on day 3.

We introduced L929 cells and cultured them for 3 days inside 3D printed monolithic and hybrid microfluidic devices. The visibility of L929 cells in bright-field microscopy was significantly better in hybrid devices than that in monolithic devices (Figures 8c,d and S10). Both devices have been printed with optimized parameters possessing around 76% optical transparency (Figure 2f). However, some of the cells were barely visible in monolithic devices even after overexposing the light (shown by white arrows in Figure 8c). Figure S11 also confirms that monolithic PETg devices are unsuitable for bright-field microscopy of cells mainly due to roof layers printed on the channel.

Moreover, both devices retained high cell viability for 3 days (Figure 8e–j). Ruhela et al. reported that the mean circularity value can be used to evaluate the cell morphological changes associated with attachment.²⁷ We found that the mean circularity of cells cultured in hybrid and monolithic devices was close to 0.7 on day 1 (Figure S12a,b). Moreover, the mean circularity reached close to 0.57 at the end of day 3 in both devices, suggesting a significant number of cells with spindle shape morphology in PETg microfluidic devices (Figure

S12c,d). This validates that 3D printed PETg microfluidic devices promote cell adhesion and spreading.

3.9. Versatility of the Proposed Fabrication Approach.

This section demonstrates that the same optimized parameters for PETg can be applicable to other FDM-compatible polymers to improve their optical transparency and enable bright-field microscopy of cells on them. We have cultured L929 cells on previously designed cylindrical devices (Figure 9a) fabricated with transparent PLA and PMMA filaments. The cylindrical devices were fabricated with optimized parameters, and optical microscopy images of cells were taken (Figure 9b,c). The optical transparency of PLA and PMMA after applying optimized parameters was $67.80 \pm 2.503\%$ ($p = 0.0093$ between PETg and PLA) and $79.10 \pm 2.643\%$ (nonsignificant with PETg), respectively (Figure 9d). Both the cylindrical constructs permitted excellent bright-field imaging of cells due to their improved optical transparency with optimized parameters. However, 3D printed PMMA had better optical transparency compared to PLA. The spreading morphology of L929 cells was also noticeable on both constructs. Moreover, FDA/PI staining on 3D printed devices revealed that the cells retained high

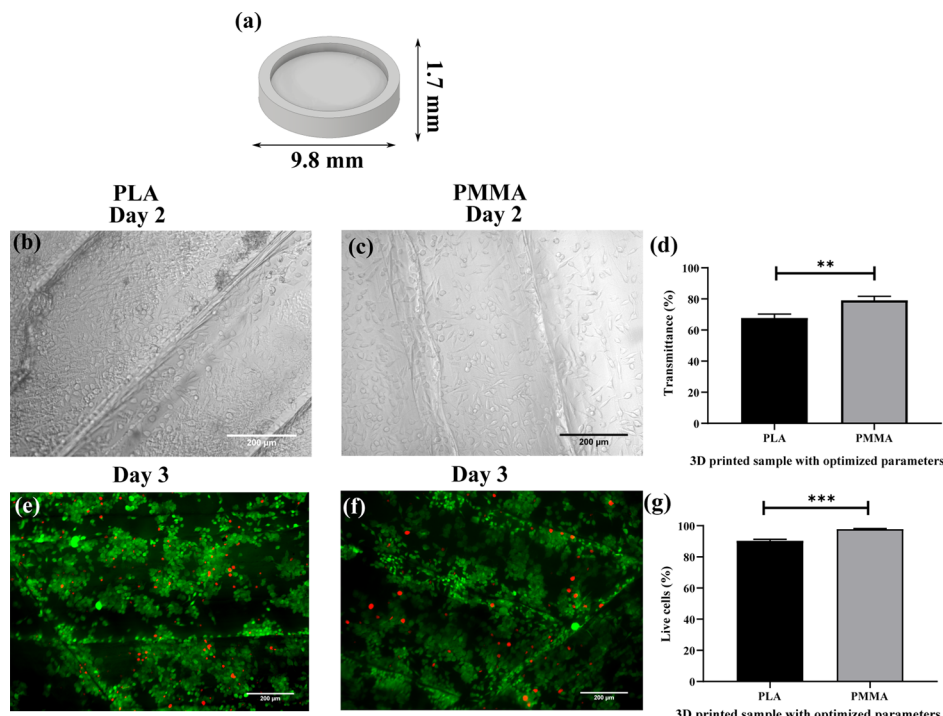


Figure 9. Cell culture on PLA and PMMA. (a) CAD model of the 3D printed device used for cell culture, (b) optical microscopy image of L929 cells cultured on PLA on day 2, (c) optical microscopy image of L929 cells cultured on PMMA on day 2, (d) optical transparency measurement of 3D printed PLA and PMMA with optimized parameters, (e) live/dead staining (FDA/PI) of L929 cells cultured on PLA on day 3, (f) live/dead staining (FDA/PI) of L929 cells cultured on PMMA on day 3, and (g) quantification of cell viability on PLA and PMMA on day 3.

viability (~90%) on both PLA and PMMA at the end of day 3 (Figure 9e–g). However, cell viability on PMMA was slightly higher than that on PLA. Hence, transparent polymers such as PMMA and PLA can also be used for fabricating biomicrofluidic devices with the proposed fabrication approach in addition to PETg.

4. DISCUSSION

In the present study, we have used filament-based polymer extrusion to fabricate optically transparent PETg-based hybrid biomicrofluidic devices. We found that reducing layer height, printing speed, cooling fan speed, and increasing extrusion flow enhanced the optical transparency of PETg devices. Moreover, transparent micromixers with complex planar and nonplanar microchannels were possible to print with FDM 3D printing. The 3D printed PETg surface, despite its low wettability, allowed cell attachment, spreading, and proliferation during 3 days of culture without ECM coating or surface treatment. PETg-based hybrid and monolithic microfluidic devices maintained high cell viability and promoted cell adhesion. However, the visibility of L929 cells in bright-field microscopy was significantly better in hybrid devices than monolithic devices. Finally, we demonstrated that the optimized parameters could be applied to other FDM-compatible polymers such as PMMA and PLA to improve their transparency and develop transparent biomicrofluidic devices from them.

The layer-by-layer approach of 3D printing inherently introduces voids among 3D printed layers, resulting in excessive light scattering and opacity.^{20,38} By optimizing the process parameters, the voids can be minimized. From Figure 2a–c, we observed light transmittance from PETg samples improved with low printing speed. This is because the material gets more time to flow into the air gaps (voids) and fuse with the adjacent fibers

with decreasing printing speed, improving the overall optical transparency of 3D printed devices.^{22,39,40}

Tothill et al. mentioned that the circular nature of printed filament increased with higher layer height, thus producing more voids among the layers.²² Contrary to the results obtained in the present study, they demonstrated the dramatic influence of layer height on transmittance. This is because they used a broader range of layer height (0.06, 0.15, 0.25 mm) and lower printing speeds (5, 7.5, 10 mm/s) than the present study, suggesting printing speeds lower than 10 mm/s may augment the effect of layer height on the transmittance of 3D printed samples. This also explains the significant influence of layer height on transmittance only at 10 mm/s (lowest printing speed) in the present study.

We found that the extrusion flow of 104% produced higher optical transparency than 100% extrusion flow (Figure 2e). This is because of excess extruded material filling the air gaps present among the rasters (fibers), thereby improving the optical transparency. However, we believe that once the extrusion flow increased beyond 104%, most of the excess extruded material got swept out toward the corners of the sample with nozzle movements, not filling the voids effectively. This might be the reason behind no further improvement in transmittance with extrusion flow higher than 104%. Therefore, we think an upper limit of light transmittance at 104% extrusion flow exists beyond which it cannot be further improved with increased extrusion flow.

The cooling fan speeds of 0, 20, and 40% substantially affected the optical transparency of the samples (Figure 2f). Lee et al. found that higher cooling speeds prevented adhesion of layers, producing more voids in the 3D printed part.⁴¹ Hence, as the cooling fan speed decreases, the extruded plastic stays at a higher temperature for a longer time, improving the fluidity of extruded

plastic. Improvement in fluidity allows the material to flow into the air gaps and fuse with the adjacent fibers, enhancing optical transparency. However, the same effect was not observed after the cooling fan speed exceeded 40%. Therefore, we recommend keeping the cooling fan speed below 40% to improve optical transparency compared to control.

As mentioned before, the air voids trapped in the layers affect the overall transparency of the samples. We found different zigzag infill orientations (infill angles) kept the optical transparency unchanged (Figure S3). However, alternate infill angles (45° , 135°) produced significantly lower transparency, suggesting they produced more voids among the layers.

Printing temperature is also known to affect voids present among the layers.⁴⁰ Hence, we believe increasing 3D printing temperature may improve the optical transparency of the samples. However, setting a higher printing temperature will increase the fluidity (lower viscosity) of molten plastic material, producing higher-dimensional variations.

From Figure 3b–g, we found that the excess material extruded around the channels resulted in the reduction of the channel width. Moreover, decreased cooling fan speed led to increased fluidity of the molten plastic, resulting in a reduced channel width (Figure 3h–m). From Figure 3o, we found that the significance level between 20 and 100% cooling fan speed was close to $p = 0.05$. Therefore, we believe that 20% cooling fan speed can also be used for printing microfluidic devices by increasing the channel width to compensate for the 3D printing dimensional error. From Figure 2f, it can be assumed that the average optical transparency will increase by 4.63% if a cooling fan speed of 20% is used instead of 40%. Besides, 110% extrusion flow produced an average channel width of $246\ \mu\text{m}$, showing a possibility to fabricate sub- $200\ \mu\text{m}$ channels using FDM by controlling extrusion flow and cooling fan speed. Although finer nozzle diameters ($<0.4\ \text{mm}$) may produce a better resolution, they require longer printing time and frequently end up being clogged. Therefore, we believe that the approach of controlling extrusion flow and cooling fan speed is better for producing sub- $200\ \mu\text{m}$ channels for low-resolution FDM 3D printers.

Previous studies revealed that layer height (or layer thickness) is one of the most influential parameters affecting the surface roughness of 3D printed samples.³³ In accordance with the previous results, we found decreasing layer thickness reduced overall surface roughness.⁴² The difference in arithmetical mean height between samples printed with 0.025 and 0.05 mm layer heights was lower than the root-mean-square height. This suggests that the 0.05 mm layer height produced a larger deviation from the mean line. The uneven surface morphology observed in profilometry was reported previously.^{10,35} Feng et al. suggested that such an uneven surface is a result of sharkskin surface instability.⁴³ Sharkskinlike surface irregularity has been reported in previous literature related to polymer extrusion.^{32,43}

Sharkskin surface on the extruded polymer is observed due to stress singularity developed at the nozzle exit, resulting in rapid tensile deformation of polymer molecules in the extrudate.³² As shown in Figure S5, the printed polymer fibers preserve the sharkskin patterns developed during extrusion, greatly reducing the optical transparency of the top surface. We postulate that low cooling fan speed in optimized parameters significantly affected the temperature of the outermost part of the extruded polymer at the nozzle exit, thus reducing sharkskin development on extrudate. This hypothesis is supported by the previous study, which investigated the reduction in sharkskin roughness by controlling the temperature of the extrudate at the nozzle exit.³²

Li et al. investigated the mixing process in 3D printed mixers in detail.⁴⁴ They printed T channel micromixers with an infill angle of 30° , an extrusion width of $250\ \mu\text{m}$, and a layer height of $100\ \mu\text{m}$. They obtained 100% mixing at $25\ \mu\text{L}/\text{min}$ flow rate in the T channel device having an overall length of 20 mm (same length as designed in this study). However, the extent of mixing in our case was ~77%, with a flow rate of $10\ \mu\text{L}/\text{min}$ in the T channel mixer (Figure 5d). As discussed previously, the average surface roughness with a layer height of $100\ \mu\text{m}$ was significantly higher than $25\ \mu\text{m}$ (Figure 4). We believe that the higher surface roughness might be responsible for enhanced mixing in their case. Moreover, other parameters responsible for this mixing variation can be (1) an infill angle of 45° (not studied by them), (2) different diffusion coefficients of dyes, (3) different channel cross sections (semielliptical in our case), and (4) different extrusion widths (we used an extrusion width of $400\ \mu\text{m}$). Moreover, we hypothesize that the mixing in 3D printed semielliptical channels is mainly governed by diffusion in central and wall regions but chaotic advection in the bottom surface region due to large peaks and valleys (Figure 4), causing additional flow interfaces.^{21,45}

The contact angle of native PETg ($85 \pm 0.38^\circ$) was slightly different compared to the previously reported values of 80 and 78° .^{18,46} The contact angles reported in the present study are apparent contact angles measured on the 3D printed rough surface.⁴⁷ However, the Young contact angle (the equilibrium contact angle of the unattainable smooth surface or ideal surface) will be slightly higher in our case as predicted by Wenzel's equation.⁴⁸

Oxidation of various polymers by UV/ozone treatment has been studied widely.^{49,50} UV/ozone produces oxygen-containing functional groups like hydroxyl, carbonyl, and carboxylic acid in the polymer, increasing the polymer wettability.^{37,49} Charpentier et al. demonstrated an increase in atomic oxygen content and oxygen-containing functional groups after UV/ozone treatment of PETg.⁴⁶ In line with their results, we found that an increase in UV/ozone treatment time produced a 3D printed PETg surface with higher wettability. As microfluidic devices are often sterilized with ethanol and washed with a cell culture medium, it is necessary to characterize the resulting wettability after washing. The remaining hydrophilicity on the surface after washing has been measured as suggested by Tsao et al.⁴⁹ In agreement with the previous studies, we found washing of UV/ozone-treated surfaces produced higher contact angles, which is because of the removal of low-molecular-weight oxidized material (such as esters, acids, and carbonyls) generated during UV/ozone treatment.^{37,49,51} The remaining surface will have more stable higher-molecular-weight oxidized material such as hydroxyl groups and water-insoluble species, maintaining higher hydrophilicity than the native surface for a longer time.

The wettability of 3D printed PETg is lower than that of PET.⁵² The cellular attachment, spreading, and proliferation observed in our case contradict the requirement of moderate hydrophilicity on the surface for better cell attachment and spreading.^{48,53} However, previous studies based on FDM and selective laser melting (SLM) discussed the influence of micron-level surface roughness produced by 3D printing on enhanced cell attachment, spreading, and proliferation. Han et al. demonstrated enhanced cell proliferation and metabolic activity on highly rough 3D printed PEEK surfaces ($R_a = 22.28 \pm 15.26\ \mu\text{m}$) despite its low wettability (contact angle $84.6 \pm 9.6^\circ$) compared to other smoother PEEK surfaces.³⁵ Titanium

implants fabricated by the SLM technique with a roughness of $10.65 \pm 2.3 \mu\text{m}$ and a contact angle of $86.97 \pm 2.65^\circ$ supported better cell adhesion, proliferation, and osteoblast differentiation compared to smooth machined implants.³⁶

Usually, hydrophobic PDMS microfluidic devices require surface treatment or ECM coating to facilitate cell adhesion on their surface.⁵⁴ However, a study carried out by Ozbulat et al. revealed that 3D printed PDMS allows cell adhesion without ECM coating.⁵⁵ They mentioned that the uneven rough surface produced by 3D printing allowed cell attachment on hydrophobic PDMS. Therefore, we believe that the uneven rough surface of 3D printed PETg might have promoted cell attachment. Moreover, upregulated secretion of adhesion-promoting proteins like fibronectin and collagen by L929 cells and adsorption of ECM proteins from complete cell culture medium on the PETg rough surface also may have induced cell attachment.^{55,56}

Direct cell adhesion observed in the present study is a significant advantage of extrusion-based 3D printing over resin-based stereolithography. Previous stereolithography-based approaches required incubating microchannels with cell culture medium or surface treatment before cell seeding to induce cell attachment.^{9,57}

Like hybrid devices, we found that the cells cultured in low-gas-permeable monolithic PETg devices maintained high viability for 3 days, contradicting our hypothesis. Vogler et al. found oxygen concentration affected metabolism, spreading, morphology, and migration of L929 fibroblasts.⁵⁸ They found that hypoxic conditions led to increased cell area and more number of focal contacts in L929 in 24 h. Therefore, we expected that a higher number of focal contacts, altered morphology, and higher cell surface area if the PETg hybrid and monolithic devices do not maintain normoxia during 3 days at standard incubation conditions. However, cells appeared to maintain spindle-shaped morphology similar to cells cultured outside the microfluidic device, suggesting that both the microfluidic devices might have maintained normoxia in static conditions.

Previous studies carried out by Mehta et al.,²⁴ McMillan et al.,⁵⁹ and Trinh et al.⁶⁰ found that the cells cultured in monolayer remained viable for 3 days to 1 week in thermoplastic polymer devices. Moreover, Jeon et al. found that human microvascular endothelial cells (hMVECs) retained high cell viability for 3 days, similar to PDMS devices during monolayer culture in thermoplastic polymer microfluidic devices.⁶¹ These studies explain the high cell viability obtained at the end of day 3 in monolithic PETg devices despite its low gas permeability. Moreover, these studies also indicate that the low gas permeability of thermoplastic polymers may not pose problems for biological studies involving only monolayer cell culture for 3 days to 1 week. However, low gas permeability might present a significant challenge for studies involving 3D cell culture (spheroid culture or cell culture inside hydrogels). Therefore, we believe that further study with 3D spheroid culture is required to validate the effectiveness of the hybrid approach over monolithic devices. Besides, regular cell culture media change (24 h) inside monolithic devices also helped to maintain normal oxygen levels and high cell viability inside PETg monolithic devices.

Although there was no difference in cell viability between hybrid and monolithic devices, the optical transparency of monolithic devices was found as a limitation. Both the devices were printed with optimized parameters, but the roof layers in

monolithic devices reduced the cell visibility in bright-field microscopy. Therefore, it is necessary to use a hybrid concept to enable bright-field microscopy in filament extrusion-based devices in addition to optimized parameters.

Finally, when the optimized parameters were applied to PMMA and PLA, we found that the optical transparency of PMMA was significantly higher than PLA. This is because clear PLA filaments have a yellowish hue. Therefore, apart from the optimization of parameters, the natural transparency of filament is also important. The high cell viability on PLA and PMMA is in line with previous results of cell culture on FDM-based polymers.^{60,62} The same hybrid concept and optimized parameters can be applied for developing 3D printed transparent biomicrofluidic devices out of PLA and PMMA.

5. CONCLUSIONS

In this study, we have 3D printed exceptionally transparent and biocompatible PETg-based hybrid microfluidic devices allowing bright-field microscopy of cells and promoting cell attachment. To the best of our knowledge, this is the first study reporting fabrication and cell culture inside 3D printed PETg biomicrofluidic devices. We have also demonstrated the influence of extrusion flow and cooling fan speed on optical transparency of the 3D printed samples, previously not discussed. Optimization of 3D printing parameters yielded optical transparency close to 80% in 3D printed microfluidic devices, which was not achievable before. Moreover, optimized parameters also reduced sharkskin surface roughness significantly. Using the optimized parameters, we have demonstrated 3D printing of various transparent microfluidic mixing devices. Especially, the fabrication of a 3D mixer with a nonplanar channel network was demonstrated, which is not feasible to fabricate with conventional soft lithography. We have found that wettability of PETg can be controlled easily with UV/ozone surface activation. Despite the low wettability, 3D printed native PETg surfaces allowed cell attachment, spreading, and proliferation without ECM coating or surface treatment. This might be due to its rough and uneven surface, promoting cell adhesion and upregulating cell secretion of adhesion-promoting proteins. Cells cultured in hybrid PETg-PDMS and monolithic PETg biomicrofluidic devices maintained high viability without altered cell morphology, indicating the devices possibly maintained normoxia during 3 days of cell culture. Although both the devices maintained high cell viability, the optical transparency of monolithic devices was significantly lower than hybrid devices, not suitable for optical microscopy of cells. Finally, we have applied the optimized parameters to other FDM-compatible polymers such as PMMA and PLA to demonstrate the versatility of the proposed fabrication approach. We have found that the cells were visible in bright-field microscopy on both materials because of their improved optical transparency with optimized parameters. Moreover, cells maintained high viability on PLA and PMMA, showing their applicability as 3D printed biomicrofluidic device material. The low-cost 3D printed hybrid biomicrofluidic devices can be used for long-term cell culture, anticancer drug testing, and other biological applications. Our future work includes 3D spheroid-based anticancer drug testing and multicell interaction for studying cancer metastasis inside 3D printed microfluidic devices.

■ ASSOCIATED CONTENT

SI Supporting Information

The Supporting Information is available free of charge at <https://pubs.acs.org/doi/10.1021/acsbiomaterials.1c00633>.

Transmittance in the visible light spectrum for each printing speed at 0.025 mm layer height (Figure S1), images of 3D printed PETg samples showing variation in optical transparency (Figure S2), effect of infill angle on optical transparency of PETg samples (Figure S3), nozzle movement path for zigzag infill (45°) for various 3D printed devices (Figure S4), sharkskin surface roughness on 3D printed PETg (Figure S5), cross sections of 3D printed microchannels (Figure S6), CAD models of microfluidic mixers (Figure S7), 3D printed micromixers with blue dye perfusion (Figure S8), comparison of optical transparency of 3D printed microchannels without roof layers and with roof layers (Figure S9), L929 fibroblasts cultured in hybrid PETg-PDMS biomicrofluidic devices (Figure S10), L929 fibroblasts cultured in monolithic PETg biomicrofluidic devices (Figure S11), circularity analysis of cells cultured in hybrid and monolithic devices (Figure S12), and printing time for microfluidic devices used in this study (Table S1) ([PDF](#))

Blue dye perfusion in the permanently bonded hybrid microfluidic device (Video S1) ([AVI](#))

■ AUTHOR INFORMATION

Corresponding Author

Subha Narayan Rath – *Regenerative Medicine and Stem Cell Laboratory (RMS), Department of Biomedical Engineering, Indian Institute of Technology Hyderabad (IITH), Sangareddy 502285 Telangana, India; Phone: +91 40 2301 6103; Email: subharath@bme.iith.ac.in; Fax: +91 40 2301 6032*

Authors

Viraj Mehta – *Regenerative Medicine and Stem Cell Laboratory (RMS), Department of Biomedical Engineering, Indian Institute of Technology Hyderabad (IITH), Sangareddy 502285 Telangana, India;  orcid.org/0000-0003-1153-1205*

Sukanya Vilikkathala Sudhakaran – *Regenerative Medicine and Stem Cell Laboratory (RMS), Department of Biomedical Engineering, Indian Institute of Technology Hyderabad (IITH), Sangareddy 502285 Telangana, India*

Complete contact information is available at:
<https://pubs.acs.org/10.1021/acsbiomaterials.1c00633>

Notes

The authors declare no competing financial interest.

■ ACKNOWLEDGMENTS

V.M. is supported by the Prime Minister's Research Fellowship (PMRF) provided by the Ministry of Human Resource Development (MHRD, Govt. of India). S.V.S. is supported by the Council of Scientific and Industrial Research Fellowship (CSIR, India). This work was funded by PMRF, MHRD, India. We thank the National Centre for Cell Science (NCCS, Pune, India) for providing the L929 cell line.

■ REFERENCES

- (1) Huh, D.; Torisawa, Y. S.; Hamilton, G. A.; Kim, H. J.; Ingber, D. E. Microengineered Physiological Biomimicry: Organs-on-Chips. *Lab Chip* **2012**, *12*, 2156–2164.
- (2) Dhiman, N.; Shagagh, N.; Bhave, M.; Sumer, H.; Kingshott, P.; Rath, S. N. Selective Cytotoxicity of a Novel Trp-Rich Peptide against Lung Tumor Spheroids Encapsulated inside a 3D Microfluidic Device. *Adv. Biosyst.* **2020**, *4*, No. 1900285.
- (3) Dhiman, N.; Kingshott, P.; Sumer, H.; Sharma, C. S.; Rath, S. N. On-Chip Anticancer Drug Screening – Recent Progress in Microfluidic Platforms to Address Challenges in Chemotherapy. *Biosens. Bioelectron.* **2019**, *137*, 236–254.
- (4) Au, A. K.; Huynh, W.; Horowitz, L. F.; Folch, A. 3D-Printed Microfluidics. *Angew. Chem., Int. Ed.* **2016**, *55*, 3862–3881.
- (5) Sankar, S.; Kakunuri, M.; D Eswaramoorthy, S.; Sharma, C. S.; Rath, S. N. Effect of Patterned Electrospun Hierarchical Structures on Alignment and Differentiation of Mesenchymal Stem Cells: Biomimicking Bone. *J. Tissue Eng. Regener. Med.* **2018**, *12*, e2073–e2084.
- (6) Mehta, V.; Rath, S. N. 3D Printed Microfluidic Devices: A Review Focused on Four Fundamental Manufacturing Approaches and Implications on the Field of Healthcare. *Bio-Des. Manuf.* **2021**, *4*, 311–343.
- (7) Chan, H. N.; Chen, Y.; Shu, Y.; Chen, Y.; Tian, Q.; Wu, H. Direct, One-Step Molding of 3D-Printed Structures for Convenient Fabrication of Truly 3D PDMS Microfluidic Chips. *Microfluid. Nanofluid.* **2015**, *19*, 9–18.
- (8) Enders, A.; Siller, I. G.; Urmann, K.; Hoffmann, M. R.; Bahnemann, J. 3D Printed Microfluidic Mixers—A Comparative Study on Mixing Unit Performances. *Small* **2019**, *15*, No. 1804326.
- (9) Kuo, A. P.; Bhattacharjee, N.; Lee, Y. S.; Castro, K.; Kim, Y. T.; Folch, A. High-Precision Stereolithography of Biomicrofluidic Devices. *Adv. Mater. Technol.* **2019**, *4*, No. 1800395.
- (10) Morgan, A. J. L.; San Jose, L. H.; Jamieson, W. D.; Wymant, J. M.; Song, B.; Stephens, P.; Barrow, D. A.; Castell, O. K. Simple and Versatile 3D Printed Microfluidics Using Fused Filament Fabrication. *PLoS One* **2016**, *11*, No. e0152023.
- (11) Li, F.; Smejkal, P.; Macdonald, N. P.; Guijt, R. M.; Breadmore, M. C. One-Step Fabrication of a Microfluidic Device with an Integrated Membrane and Embedded Reagents by Multimaterial 3D Printing. *Anal. Chem.* **2017**, *89*, 4701–4707.
- (12) Bressan, L. P.; Adamo, C. B.; Quero, R. F.; De Jesus, D. P.; Da Silva, J. A. F. A Simple Procedure to Produce FDM-Based 3D-Printed Microfluidic Devices with an Integrated PMMA Optical Window. *Anal. Methods* **2019**, *11*, 1014–1020.
- (13) Duong, L. H.; Chen, P. C. Simple and Low-Cost Production of Hybrid 3D-Printed Microfluidic Devices. *Biomicrofluidics* **2019**, No. 024108.
- (14) Tsuda, S.; Jaffery, H.; Doran, D.; Hezwani, M.; Robbins, P. J.; Yoshida, M.; Cronin, L. Customizable 3D Printed ‘Plug and Play’ Millifluidic Devices for Programmable Fluidics. *PLoS One* **2015**, *10*, No. e0141640.
- (15) Bressan, L. P.; Lima, T. M.; da Silveira, G. D.; da Silva, J. A. F. Low-Cost and Simple FDM-Based 3D-Printed Microfluidic Device for the Synthesis of Metallic Core–Shell Nanoparticles. *SN Appl. Sci.* **2020**, *2*, No. 984.
- (16) Lee, H.; Cho, D. W. One-Step Fabrication of an Organ-on-a-Chip with Spatial Heterogeneity Using a 3D Bioprinting Technology. *Lab Chip* **2016**, *16*, 2618–2625.
- (17) Nie, J.; Gao, Q.; Qiu, J. J.; Sun, M.; Liu, A.; Shao, L.; Fu, J. Z.; Zhao, P.; He, Y. 3D Printed Lego -like Modular Microfluidic Devices Based on Capillary Driving. *Biofabrication* **2018**, *10*, No. 035001.
- (18) Chen, T.; Zhang, J. Surface Hydrophilic Modification of Acrylonitrile-Butadiene-Styrene Terpolymer by Poly(Ethylene Glycol-Co-1,4-Cyclohexanedimethanol Terephthalate): Preparation, Characterization, and Properties Studies. *Appl. Surf. Sci.* **2016**, *388*, 133–140.
- (19) Guima, K. E.; Coelho, P. H. L.; Trindade, M. A. G.; Martins, C. A. 3D-Printed Glycerol Microfluidic Fuel Cell. *Lab Chip* **2020**, *20*, 2057–2061.

- (20) Romanov, V.; Samuel, R.; Chaharlang, M.; Jafek, A. R.; Frost, A.; Gale, B. K. FDM 3D Printing of High-Pressure, Heat-Resistant, Transparent Microfluidic Devices. *Anal. Chem.* **2018**, *90*, 10450–10456.
- (21) Macdonald, N. P.; Cabot, J. M.; Smejkal, P.; Guijt, R. M.; Paull, B.; Breadmore, M. C. Comparing Microfluidic Performance of Three-Dimensional (3D) Printing Platforms. *Anal. Chem.* **2017**, *89*, 3858–3866.
- (22) Tothill, A. M.; Partridge, M.; James, S. W.; Tatam, R. P. Fabrication and Optimisation of a Fused Filament 3D-Printed Microfluidic Platform. *J. Micromech. Microeng.* **2017**, *27*, No. 035018.
- (23) Yuen, P. K. Embedding Objects during 3D Printing to Add New Functionalities. *Biomicrofluidics* **2016**, *10*, No. 044104.
- (24) Mehta, G.; Lee, J.; Cha, W.; Tung, Y. C.; Linderman, J. J.; Takayama, S. Hard Top Soft Bottom Microfluidic Devices for Cell Culture and Chemical Analysis. *Anal. Chem.* **2009**, *81*, 3714–3722.
- (25) Beckwith, A. L.; Borenstein, J. T.; Velasquez-Garcia, L. F. Monolithic, 3D-Printed Microfluidic Platform for Recapitulation of Dynamic Tumor Microenvironments. *J. Microelectromech. Syst.* **2018**, *27*, 1009–1022.
- (26) Sip, C. G.; Folch, A. Stable Chemical Bonding of Porous Membranes and Poly(Dimethylsiloxane) Devices for Long-Term Cell Culture. *Biomicrofluidics* **2014**, *8*, No. 036504.
- (27) Ruhela, A.; Kasinathan, G. N.; Rath, S. N.; Sasikala, M.; Sharma, C. S. Electrospun Freestanding Hydrophobic Fabric as a Potential Polymer Semi-Permeable Membrane for Islet Encapsulation. *Mater. Sci. Eng., C* **2021**, *118*, No. 111409.
- (28) Mohan Pandey, P.; Venkata Reddy, N.; Dhande, S. G. Slicing Procedures in Layered Manufacturing: A Review. *Rapid Prototyping J.* **2003**, *9*, 274–288.
- (29) Kotz, F.; Mader, M.; Dellen, N.; Risch, P.; Kick, A.; Helmer, D.; Rapp, B. Fused Deposition Modeling of Microfluidic Chips in Polymethylmethacrylate. *Micromachines* **2020**, *11*, No. 873.
- (30) Kuo, J. S.; Ng, L.; Yen, G. S.; Lorenz, R. M.; Schiro, P. G.; Edgar, J. S.; Zhao, Y.; Lim, D. S. W.; Allen, P. B.; Jeffries, G. D. M.; Chiu, D. T. A New USP Class VI-Compliant Substrate for Manufacturing Disposable Microfluidic Devices. *Lab Chip* **2009**, *9*, 870–876.
- (31) Nelson, M. D.; Ramkumar, N.; Gale, B. K. Flexible, Transparent, Sub-100 Mm Microfluidic Channels with Fused Deposition Modeling 3D-Printed Thermoplastic Polyurethane. *J. Micromech. Microeng.* **2019**, *29*, No. 095010.
- (32) Miller, E.; Rothstein, J. P. Control of the Sharkskin Instability in the Extrusion of Polymer Melts Using Induced Temperature Gradients. *Rheol. Acta* **2004**, *44*, 160–173.
- (33) Jaisingh Sheoran, A.; Kumar, H. Fused Deposition Modeling Process Parameters Optimization and Effect on Mechanical Properties and Part Quality: Review and Reflection on Present Research. *Mater. Today: Proc.* **2020**, *21*, 1659–1672.
- (34) Bhattacharjee, N.; Urrios, A.; Kang, S.; Folch, A. The Upcoming 3D-Printing Revolution in Microfluidics. *Lab Chip* **2016**, *16*, 1720–1742.
- (35) Han, X.; Sharma, N.; Xu, Z.; Scheideler, L.; Geis-Gerstorfer, J.; Rupp, F.; Thieringer, F. M.; Spintzyk, S. An In Vitro Study of Osteoblast Response on Fused-Filament Fabrication 3D Printed PEEK for Dental and Cranio-Maxillofacial Implants. *J. Clin. Med.* **2019**, *8*, No. 771.
- (36) Shaoki, A.; Xu, J. Y.; Sun, H.; Chen, X. S.; Ouyang, J.; Zhuang, X. M.; Deng, F. L. Osseointegration of Three-Dimensional Designed Titanium Implants Manufactured by Selective Laser Melting. *Biofabrication* **2016**, *8*, No. 045014.
- (37) Teare, D. O. H.; Emmison, N.; Ton-That, C.; Bradley, R. H. Cellular Attachment to Ultraviolet Ozone Modified Polystyrene Surfaces. *Langmuir* **2000**, *16*, 2818–2824.
- (38) Boschetto, A.; Bottini, L.; Veniali, F. Finishing of Fused Deposition Modeling Parts by CNC Machining. *Rob. Comput. Integr. Manuf.* **2016**, *41*, 92–101.
- (39) Wang, P.; Zou, B.; Ding, S.; Li, L.; Huang, C. Effects of FDM-3D Printing Parameters on Mechanical Properties and Microstructure of CF/PEEK and GF/PEEK. *Chin. J. Aeronaut.* **2020**, DOI: [10.1016/j.cja.2020.05.040](https://doi.org/10.1016/j.cja.2020.05.040).
- (40) Wang, P.; Zou, B.; Xiao, H.; Ding, S.; Huang, C. Effects of Printing Parameters of Fused Deposition Modeling on Mechanical Properties, Surface Quality, and Microstructure of PEEK. *J. Mater. Process. Technol.* **2019**, *271*, 62–74.
- (41) Lee, C. Y.; Liu, C. Y. The Influence of Forced-Air Cooling on a 3D Printed PLA Part Manufactured by Fused Filament Fabrication. *Addit. Manuf.* **2019**, *25*, 196–203.
- (42) Turner, B. N.; Gold, S. A. A Review of Melt Extrusion Additive Manufacturing Processes: II. Materials, Dimensional Accuracy, and Surface Roughness. *Rapid Prototyping J.* **2015**, *250*–261.
- (43) Feng, K. C.; Pinkas-Sarafova, A.; Ricotta, V.; Cuffo, M.; Zhang, L.; Guo, Y.; Chang, C. C.; Halada, G. P.; Simon, M.; Rafailovich, M. The Influence of Roughness on Stem Cell Differentiation Using 3D Printed Polylactic Acid Scaffolds. *Soft Matter* **2018**, *14*, 9838–9846.
- (44) Li, F.; Macdonald, N. P.; Guijt, R. M.; Breadmore, M. C. Using Printing Orientation for Tuning Fluidic Behavior in Microfluidic Chips Made by Fused Deposition Modeling 3D Printing. *Anal. Chem.* **2017**, *89*, 12805–12811.
- (45) Simonnet, C.; Groisman, A. Chaotic Mixing in a Steady Flow in a Microchannel. *Phys. Rev. Lett.* **2005**, *94*, No. 134501.
- (46) Charpentier, P. A.; Maguire, A.; Wan, W. K. Surface Modification of Polyester to Produce a Bacterial Cellulose-Based Vascular Prosthetic Device. *Appl. Surf. Sci.* **2006**, *252*, 6360–6367.
- (47) Meiron, T. S.; Marmur, A.; Saguy, I. S. Contact Angle Measurement on Rough Surfaces. *J. Colloid Interface Sci.* **2004**, *274*, 637–644.
- (48) Rosales-Leal, J. I.; Rodríguez-Valverde, M. A.; Mazzaglia, G.; Ramón-Torregrosa, P. J.; Díaz-Rodríguez, L.; García-Martínez, O.; Vallecillo-Capilla, M.; Ruiz, C.; Cabrerizo-Vilchez, M. A. Effect of Roughness, Wettability and Morphology of Engineered Titanium Surfaces on Osteoblast-like Cell Adhesion. *Colloids Surf., A* **2010**, *365*, 222–229.
- (49) Tsao, C. W.; Hromada, L.; Liu, J.; Kumar, P.; DeVoe, D. L. Low Temperature Bonding of PMMA and COC Microfluidic Substrates Using UV/Ozone Surface Treatment. *Lab Chip* **2007**, *7*, 499–505.
- (50) Van Midwoud, P. M.; Janse, A.; Merema, M. T.; Groothuis, G. M. M.; Verpoorte, E. Comparison of Biocompatibility and Adsorption Properties of Different Plastics for Advanced Microfluidic Cell and Tissue Culture Models. *Anal. Chem.* **2012**, *84*, 3938–3944.
- (51) Teare, D. O. H.; Ton-That, C.; Bradley, R. H. Surface Characterization and Ageing of Ultraviolet-Ozone-Treated Polymers Using Atomic Force Microscopy and x-Ray Photoelectron Spectroscopy. *Surf. Interface Anal.* **2000**, *29*, 276–283.
- (52) Dadsetan, M.; Mirzadeh, H.; Sharifi-Sanjani, N.; Daliri, M. Cell Behavior on Laser Surface-Modified Polyethylene Terephthalate in Vitro. *J. Biomed. Mater. Res.* **2001**, *57*, 183–189.
- (53) Lee, J. H.; Khang, G.; Lee, J. W.; Lee, H. B. Interaction of Different Types of Cells on Polymer Surfaces with Wettability Gradient. *J. Colloid Interface Sci.* **1998**, *205*, 323–330.
- (54) Kang, Y. B. A.; Eo, J.; Mert, S.; Yarmush, M. L.; Usta, O. B. Metabolic Patterning on a Chip: Towards in Vitro Liver Zonation of Primary Rat and Human Hepatocytes. *Sci. Rep.* **2018**, *8*, No. 8951.
- (55) Ozbolat, V.; Dey, M.; Ayan, B.; Povilianskas, A.; Demirel, M. C.; Ozbolat, I. T. 3D Printing of PDMS Improves Its Mechanical and Cell Adhesion Properties. *ACS Biomater. Sci. Eng.* **2018**, *4*, 682–693.
- (56) Lampin, M.; Warocquier-Clérout, R.; Legris, C.; Degrange, M.; Sigot-Luizard, M. F. Correlation between Substratum Roughness and Wettability, Cell Adhesion, and Cell Migration. *J. Biomed. Mater. Res.* **1997**, *36*, 99–108.
- (57) Urrios, A.; Parra-Cabrera, C.; Bhattacharjee, N.; Gonzalez-Suarez, A. M.; Rigat-Brugarolas, L. G.; Nallapatti, U.; Samitier, J.; Deforest, C. A.; Posas, F.; Garcia-Cordero, J. L.; Folch, A. 3D-Printing of Transparent Bio-Microfluidic Devices in PEG-DA. *Lab Chip* **2016**, *16*, 2287–2294.
- (58) Vogler, M.; Vogel, S.; Krull, S.; Farhat, K.; Leisering, P.; Lutz, S.; Wuertz, C. M.; Katschinski, D. M.; Zieseniss, A. Hypoxia Modulates Fibroblastic Architecture, Adhesion and Migration: A Role for HIF-1 α in Cofilin Regulation and Cytoplasmic Actin Distribution. *PLoS One* **2013**, *8*, No. e69128.

- (59) McMillan, A. H.; Thomée, E. K.; Dellaquila, A.; Nassman, H.; Segura, T.; Lesher-Pérez, S. C. Rapid Fabrication of Membrane-Integrated Thermoplastic Elastomer Microfluidic Devices. *Micro-machines* **2020**, *11*, No. 731.
- (60) Trinh, K. T. L.; Thai, D. A.; Chae, W. R.; Lee, N. Y. Rapid Fabrication of Poly(Methyl Methacrylate) Devices for Lab-On-a-Chip Applications Using Acetic Acid and UV Treatment. *ACS Omega* **2020**, *5*, 17396–17404.
- (61) Jeon, J. S.; Chung, S.; Kamm, R. D.; Charest, J. L. Hot Embossing for Fabrication of a Microfluidic 3D Cell Culture Platform. *Biomed. Microdevices* **2011**, *13*, 325–333.
- (62) Salentijn, G. I. J.; Oomen, P. E.; Grajewski, M.; Verpoorte, E. Fused Deposition Modeling 3D Printing for (Bio)Analytical Device Fabrication: Procedures, Materials, and Applications. *Anal. Chem.* **2017**, *89*, 7053–7061.